

SCUOLA DI INGEGNERIA INDUSTRIALE E DELL'INFORMAZIONE

Preliminary solar field design accounting for heliostat field status and aiming strategies in solar tower plants

Tesi di Laurea Magistrale in Energy Engineering - Ingegneria Energetica

Chiara Lupi, 987105

Abstract: Solar Tower power plants face significant challenges to ensure their worldwide deployment, including heliostat soiling leading to optical efficiency degradation and increased operation and maintenance costs due to cleaning operations. Additionally, optimizing the thermal power output of the receiver is crucial and depends on the selected aiming strategy, directly affecting receiver thermal efficiency and operational lifetime.

To tackle these issues, this research proposes a methodology for the preliminary design of Solar Tower power plants' solar fields. This methodology integrates a physical model to simulate soiling losses and optimizes cleaning schedules using a fixed-frequency time-based heuristic method. After selecting the desired aiming strategy, SolarPILOT is utilized alongside a heuristic defocusing and re-focusing strategy to simulate plant performance. Moreover, drivers failure analysis is considered for improved accuracy.

Applied to Solar Tower facilities in Mount Isa, Queensland, Australia, the methodology analyzes various solar field sizes to identify the configuration with the lowest Levelized Cost of Electricity. Results show that oversizing the solar field by five times and coupling it with a 6.5-hours Thermal Energy Storage system is optimal for turbine full-load operation, while oversizing by four times and coupling with an 11.5-hours storage system is optimal for load-based operation. A sensitivity analysis on heliostat pricing reveals a drop in field oversizing by one size when the price doubles, regardless of dispatching strategies and field cleaning conditions. In conclusion, this research contributes to the development of a comprehensive

In conclusion, this research contributes to the development of a comprehensive sizing methodology for Solar Tower power plants, integrating soiling and aiming strategies and highlighting the impact of heliostat pricing and dispatching strategies on plant performance and economics.

Advisor: Prof. Giampaolo Manzolini

Co-advisors:

Prof. Michael Cholette

Academic year: 2022-2023

Key-words: CSP, solar tower, solar field, soiling, heliostats cleaning, aiming strategy

1. Introduction

The energy transition requires a rapid expansion of electricity generation from renewable sources. According to the International Energy Agency (IEA) 1.5° Scenario, the global share of renewables in the power generation mix is expected to grow from 28% to 91%, between 2020 and 2050 [1]. In such context, Concentrated Solar Power (CSP) plants emerge as a promising technology, whose Levelized Cost of Electricity (LCOE) has experienced a

significant 69% drop, from 0.380 USD/kWh in 2010 to 0.118 USD/kWh in 2022 [2].

While CSP plants equipped with Thermal Energy Storage (TES) enhance power system flexibility and stability, their widespread adoption remains limited, with the cumulative global capacity reaching only 6.5 GW by the end of 2022 [2]. To foster the adoption of CSP plants, reduction in installation costs, technology improvements, competitive supply chains and reduced O&M costs are needed.

Solar Towers (STs) are advantageous for their ability to achieve high solar concentration factors, operate at elevated temperatures, and exhibit increased power block efficiencies and thermal storage densities. Consequently, ST plants are expected to increase their share in the energy mix in the coming years [2]. However, they face many challenges that can hinder their worldwide deployment, one of them being heliostats soiling, which reduces the solar field optical efficiency and the power collected on the receiver, with impacts on Operation and Maintenance (O&M) costs related to heliostats cleaning [3]. In addition, the plant can be successfully operated only if the receiver damage is avoided, preserving its lifetime. A proper aiming strategy can prevent permanent receiver damage and thermal efficiency degradation, while seeking the maximization of the thermal power output [4]. Addressing these issues is therefore fundamental to ensure the competitiveness of Solar Tower plants in the renewable energy sector.

1.1. State Of The Art

A fundamental step of the design of a Solar Tower plant deals with the identification of the optimal size of the heliostat field, which represents approximately 50% of the total investment cost [5]. The solar field design is a trade-off between plant performance, power dissipation, thermal efficiency and optical efficiency, including eventual defocusing [6]. The design of efficient and cost-effective solar fields has been widely studied. The work by Rizvi et al. (2021) [7] provides a overview of the optimization methodologies employed over the past decades. **Table 1** summarizes the most relevant studies and the latest available options. They represent only a fraction of the extensive efforts dedicated to this topic.

Table 1: Summary of heliostats field optimization techniques

Reference	Obj function and variables	Algorithm	Solar field type
Collado et al. (2019) [8]	 Annual Weighted Efficiency Levelized Cost of Electricity Field layout and boundary, tower height and receiver size 	Smart search broken into two consecutive stages	Surrounding Radial Staggered
Li et al. (2018) [9]	 Annual Averaged Efficiency Annual Energy Collected per Unit Cost Daily averaged efficiency Daily energy collection 	Hybrid Particle Swarm Optimization - Genetic Algorithm	Radial Staggered with Zones
Wang et al. (2019) [10]	Row spacingPedestal heightInstantaneous optical efficiency	High Dimensional Genetic Algorithm	Surrounding Radial Staggered
Cruz et al. (2019) [11]	Power concentrated by field	HECTOR, meta-heuristic algorithm	Pattern Free Layout
Deng et al. (2020) [12]	• 43 radial spacing between rows are optimized	Dynamic Specification based Differential Evolution	Rose Pattern based on Radial Staggered Pattern
Saghafifar et al. (2019) [13]	Annual weighted efficiencyLevelized Cost of Energy	Genetic Algorithm	Radial Staggered
Schöttl et al. (2019) [14]	• Ratio of optical efficiency and ground usage	Evolutionary Algorithm	Radial Staggered bounded by a poly- gon
Yang et al. (2020) [15]	Insolation weighted optical efficiencyLevelized Cost of Electricity	Alternating direction optimization method	Radial Staggered
Ghirardi et al. (2021) [16]	Overall annual efficiencyLevelized Cost of ElectricityTower height	Heuristic two-step optimization	Radial Staggered

1.1.1. Aiming Strategies

The solar field design is strictly related to the receiver, particularly to the thermal flux collected on its surface, which in turn depends on heliostat tracking. In addition, one of the main challenges faced by Solar Tower plants is enhancing the thermal efficiency while addressing durability issues. The efficiency can be compromised by high temperature gradients and hot-spots on the receiver surface. Effective management of heliostats tracking is essential for achieving a smooth thermal flux and generating the maximum power within temperature and flux limitations. In this overview, various aiming strategies developed over the years are discussed.

Vant-Hull et al. (2002) [17] introduced the concept of Allowable Flux Density (AFD), representing the maximum flux density absorbed by the receiver without causing damage. The study underscored the significance of the aiming strategy in maintaining peak flux density below the AFD. An aimpoint management system for a plant with a cylindrical receiver, incorporating a Static Aimpoint Processing System (SAPS) and a Dynamic Aimpoint Processing System (DASP), is presented. Operational adjustments involve spreading heliostats' aimpoints vertically to reduce the peak flux and removing high-flux heliostats from tracking, ensuring safe plant operation but not optimizing the power delivery to the receiver.

Building on this work, Sánchez et al. (2017, 2018) [18, 19] extended the aiming strategy for a cylindrical receiver with the goal of maximizing the thermal power output. This approach includes a Search Algorithm to determine the maximum aiming factor for each solar field sector and a Fit Algorithm to match the symmetric flux density profile with the decreasing AFD profile along the Heat Transfer Fluid (HTF) path.

García et al. (2017) [20] integrated the AFD-based model proposed by Sánchez et al. (2017) [18] into a closed-loop control strategy. The study aimed to minimize the difference between the maximum flux and the AFD at that point. Proportional Integral Derivative (PID) controllers were implemented for each group in the heliostat field, facilitating effective distribution of flux density on the receiver while adhering to AFD limits.

Many meta-heuristic optimization techniques for heliostat tracking have been explored over the years. Cruz et al. (2016) [21] formulated a two-layered optimization problem. A meta-heuristic algorithm selected the subset of heliostats to be activated and a local gradient-based optimizer identified optimal pairings of heliostats and aiming points. The objective function aimed to minimize the discrepancy between the desired flux on the receiver and the flux generated by the chosen configuration.

Salomé et al. (2013) [22] proposed an open-loop strategy coupled with a TABU meta-heuristic optimizer for a cavity receiver solar tower. The objective was to flatten the distribution of thermal flux on the receiver, minimizing spillage losses. The study highlighted that the quantity of aiming points had no significant impact on the results, with heliostat tracking errors and aperture size identified as primary limiting factors.

Baserati et al. (2014) [23] employed a genetic algorithm to optimize the aiming strategy, aiming to minimize the standard deviation of flux density on the receiver surface. An important insight was the recognition that the size of the absorber surface must be chosen considering the material properties, as a smaller aiming surface resulted in increased interception efficiency but also higher maximum flux density.

Belhomme et al. (2014) [24] presented a meta-heuristic approach for optimizing the aiming strategy of a concentrated photovoltaic (CPV) receiver, using the Ant Colony Optimization (ACO) meta-heuristic. The same approach was then extended to a flat plate receiver Solar Tower. Recognizing the lengthy optimization time associated with ACO, Oberkirsch et al. (2023) [25] introduced improvements by pre-computing flux maps, grouping heliostats, and providing an initial solution to ACO, significantly reducing computational time.

In contrast to meta-heuristic methods, Astolfi et al. (2017) [26] introduced a deterministic optimization approach focused on reducing the peak flux on the receiver. The solar field and receiver were divided into sectors, with heliostats in the same sector aiming at the same coordinate on the vertical line facing them. The objective function aimed to minimize the differences between the maximum flux on the receiver vertical line and the ideal uniformly spread flux. Four approaches were proposed, the most efficient ones considering overlapping between sectors, effectively flattening the flux distribution and reducing peak flux.

Ashley et al. (2017) [27] also applied a deterministic approach to optimize a flat plate receiver using Binary Integer Linear Programming (BILP). A grid of aimpoints on the receiver surface was considered, with the objective of maximizing the total incident energy, incorporating constraints to limit minimum and maximum energy deliveries, as well as the energy difference between adjacent aimpoints. The study revealed that heliostats aiming at the center of the receiver exhibit lower efficiencies, while those at the edges have higher efficiencies.

1.1.2. Soiling Losses and Cleaning Strategies

The solar field can contribute up to 40% of solar energy losses [5], which are enhanced by heliostat soiling. The decrease in mirror cleanliness leads to a loss in reflectance, consequently degrading performance because the incoming Direct Normal Irradiance (DNI) can not be effectively reflected towards the receiver. Soiling also

weights on O&M costs, due to the expensive cleaning procedure. Typical O&M costs for CSP plants range between 0.02 USD/kWh and 0.04 USD/kWh, representing about 18% to 20% of the LCOE [2], and mirrors cleaning is often the predominant component [28]. In this overview, the soiling phenomenon is firstly described and assessed, then several cleaning policies are summarized.

The majority of the studies dealing with soiling characterization in CSP plants are related to experimental and statistical analysis. A summary is presented in **Table 2**.

Table 2: Summary of soiling experimental studies

Reference	Content
Griffith et al. (2014) [29]	 Periodic reflectivity measurements on samples with various exposures and tilts. Reflectivity loss calculation as the ratio between the average pixel value in the contaminated image and the average pixel value in the clean reference.
Merrouni et al. (2015) [30]	 Periodic reflectivity measurements on glass mirrors and aluminium samples, with various exposures and tilt angles. Cleanliness is the ratio between the mirror reflectivity in dirty and in clean state.
Merrouni et al. (2020) [31]	 Periodic reflectivity measurements on mirror samples. Average soiling rate calculation based on the sampling period data.
Bouaddi et al. (2015) [32]	 Periodic reflectivity measurements on mirror glass and aluminium samples. Linear Gaussian state space method describes and forecasts cleanliness.
Bouaddi et al. (2017) [33]	 Periodic reflectivity measurements on mirror glass and aluminium samples. Cleanliness factor is the ratio between the reflectivity in dirty and in clean state. Dynamic Factor Analysis (DFA) modeling changes in cumulative soiling.
Conceição et al. (2018) [34]	 Periodic reflectivity measurements on flat mirror and soiling rate calculation. Multiple linear regression model and artificial neural networks for particle deposition impact, based on environmental variables.
Bonanos et al. (2020) [35]	 Periodic reflectivity measurements. Multiple linear regression model and artificial neural networks to link soiling and environmental variables.

For the first time, in the work by Picotti et al. (2018) [36] a physical model predicting soiling on solar collectors and the consequent performance loss was described. The soiling process unfolded in a four-step sequence, referred to as the "dust life cycle" [37]. A summary is shown in **Table 3**.

Table 3: Dust life cycle summary

Generation	Deposition	Adhesion	Removal
ing into the atmosphere, involving particles lifting, global and local trans-	collectors surfaces, in- fluenced by gravity, at- mospheric turbulence,	Phenomena based on the interaction between surface and dust at the nano and micro scales: Van der Waals forces, capillarity forces, electrostatic forces, and cementation effect are involved.	on wind, gravity, and rain, counterbalancing

Considering the balance between airborne particles flow onto the surface and their removal, the soiling rate is determined. The flux of dust particles $F_{\rm d}$ is defined by **Equation 1**, where $C_{\rm d}$ represents the airborne dust concentration, $v_{\rm d}$ the deposition velocity and $\alpha_{\rm t}$ the mirror tilt angle.

$$F_{\rm d} = C_{\rm d} \cdot v_{\rm d} \cdot \cos(\alpha_{\rm t}) \tag{1}$$

Once the quantity and size distribution of dust particles on the mirror surface are established, the reflectance ρ can be expressed as per **Equation 2**. Here, ρ_0 represents the mirror reflectance in clean conditions, $A_{\rm mir}$ the mirror area, and $A_{\rm nr}$ the non-reflecting area, accounting for portions shaded by dust particles and areas where the reflected beam is blocked. Both $A_{\rm mir}$ and $A_{\rm nr}$ depend on the incidence angle θ , with higher incidents angles resulting in more shading and blocking.

$$\rho = \rho_0 \cdot \left(1 - \frac{A_{\rm nr}(\theta)}{A_{\rm mir}} \right) \tag{2}$$

In a subsequent study, Picotti et al. (2019) [38] applied the physical soiling model to all heliostats in a solar field, determining the corresponding soiling efficiency as defined in **Equation 3**. A_{hel} represents the heliostat area, and A_{soil} is the sum of shading and blocking areas. The optical efficiency η_{opt} is then computed as per **Equation 4**, where $\eta_{\text{opt,cl}}$ is the clean optical efficiency.

$$\eta_{\text{soil}} = 1 - \frac{A_{\text{soil}}}{A_{\text{hel}}} \tag{3}$$

$$\eta_{\rm opt} = \eta_{\rm opt,cl} \cdot \eta_{\rm soil}$$
(4)

The study assessed various cleaning strategies in terms of optical efficiency recovery. The results indicated diminishing marginal returns on the beneficial impact of additional cleaning. The optimal cleaning frequency was determined by balancing the extra revenues from cleaned heliostats against the cleaning costs.

The trade-off between optical efficiency recovery through cleaning activities and associated O&M costs underscores the importance of determining an optimal heliostat cleaning schedule. One of the first cleaning policies was presented by Bergeron et al. (1891) [39], describing the optimal cleaning frequency identification as an economic decision, aiming to strike a balance between increased energy production and cleaning costs. This approach had two main limitations. Firstly, it assumed a constant soiling rate, overlooking potential errors resulting from the temporal variation of soiling. Secondly, the cleaning schedules were based on fixed-time intervals, neglecting the influence of stochastic time-varying factors.

In a study by Wolfertstetter et al. (2018) [40], a time-dependent approach was introduced to address the limitations of constant soiling rate assumptions. Collector cleanliness was measured, and the soiling rate was determined at a daily resolution, revealing significant variations throughout the year. The study defined two types of cleaning schedules: threshold-based and constant. Results highlighted the increase in accuracy for time-resolved simulations. However, some limitations persisted, including the application of a uniform soiling rate to the entire solar field and the constant cleaning order of solar field loops.

The literature reviewed so far primarily addresses solar collectors. Focusing on heliostats cleaning schedules, Truong Ba et al. (2017) [41] introduced the concept of Condition-Based Maintenance. Cleaning decisions were made by comparing reflectivity with a time-varying threshold, influenced by stochastic factors like soiling rate, weather, and electricity prices. The study formulated an optimization problem as a finite-horizon Markov Decision Process, aiming to minimize the expected total maintenance cost. When compared with the time-based policy by Bergeron et al. [39], the condition-based cleaning policy by Truong Ba et al. [41] led to cost savings and reduced cleaning frequencies. However, the description of soiling as a stochastic process based on experimental data lacked a physical background.

The study by Ashley et al. (2019) [42] focused on optimizing cleaning schedules for CSP plants with the goal of maximizing energy generation. The approach involved addressing both an allocation problem, where heliostats are assigned to specific cleaning periods, and a routing problem for each time period. The heliostat field was divided into homogeneous groups, and each cluster was assigned to a cleaning period. A linear degradation function was assumed to represent mirror reflectivity loss over time, the adoption of constant soiling rates in both space and time being a strong limitation. In addition, there was an exclusive focus on energy maximization without considering the balance between costs and revenues.

Finally, the work by Picotti et al. (2020) [43] addressed some limitations of the previously described methodologies, introducing physical model-based soiling predictions [36] and an economic analysis of cleaning activities under resource constraints. The solar field was segmented into sectors, and the cleaning strategy involved determining the number of sectors to be cleaned daily, thus the deployment of trucks and crews, and the cleaning order. The objective was to minimize the Total Cleaning Cost (TCC), which comprised operating cleaning costs and degradation costs, accounting for electricity generation losses due to soiling. Two optimization strategies were examined: a simplified heuristic and Mixed-Integer Linear Programming (MILP). The latter improved the TCC by allocating resources more efficiently, concentrating the cleaning schedule where it was needed the most. An extension of this work was done in the research by Anderson et al. (2023) [44], where cleaning resources were optimized considering stochastic soiling trajectories in the initial stages of site selection and plant design, addressing implications related to operational choices.

1.1.3. Drivers Failure

When considering O&M costs, potential driver failures represent a significant component. These failures can arise from various electronic components, such as heliostat controllers and gearboxes, elevation and azimuth motors, elevation and azimuth encoders, mirror assemblies, and elevation and azimuth limit switches [45]. Accounting for heliostat reliability is crucial for a robust techno-economic assessment, yet few studies address it in the literature. For instance, Benammar et al. (2020) [46] conducted a detailed analysis of heliostat

failure probabilities, drawing on mechanics, material studies, and aerodynamics, and compared four methods for reliability analysis.

1.2. Research Objectives

Overall, aiming strategies and soiling have been thoroughly examined in the operation of solar tower plants, but their integration into the design phase is not widely explored. In this context, the proposed research establishes a methodology for preliminarily sizing the solar field, with the aim of maximizing electricity production and minimizing the Levelized Cost of Electricity, acting both on the initial investment cost and ongoing O&M costs. The focus is determining the number of heliostats to be added to the solar field, assuming fixed receiver, tower, heliostat geometries, and row spacings. The limitation of such approach is the simplification of the layout optimization to the identification of the optimal number of heliostats. However, it integrates various factors that have not been collectively considered in previous studies, including selection of aiming strategies and consideration of soiling losses. Furthermore, this research emphasizes the integration of O&M cost considerations into the design phase by optimizing heliostat cleaning procedures and accounting for associated cleaning costs. Additionally, a driver failure analysis is integrated for a more comprehensive techno-economic assessment. To the authors' knowledge, this is the first study to simultaneously account for heliostat cleaning and failure, and related O&M costs, during the design phase. The aim is to develop a robust methodology that enhances the efficacy of solar field size selection.

2. Methods

The flowchart of the methodology developed in this project to optimize the solar field design is illustrated in **Figure 1**. It delineates the steps described in the following sections.

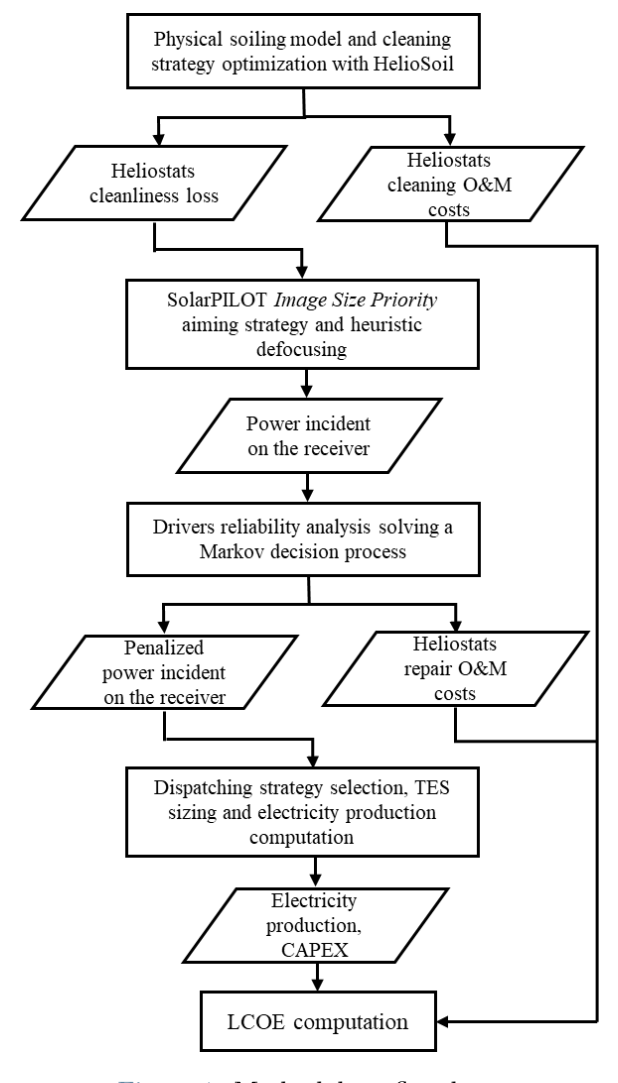


Figure 1: Methodology flowchart

The optimization of aiming strategy and characterization of receiver thermal flux are performed using SolarPILOT (Solar Power Tower Integrated Layout and Optimization Tool) coupled with a heuristic defocusing strategy. This approach is elaborated upon in **Section 2.2** and is chosen as the reference method for this research, after dismissing HALOS (Heliostat Aimpoint and Layout Optimization Software). HALOS displays inconsistencies in generating flux maps, making it unsuitable for adoption. Further details are discussed in **Section 2.1**. Furthermore, soiling model and cleaning strategy optimization methodology with HelioSoil are described (**Section 2.3**), as well as drivers reliability analysis (**Section 2.4**). Two options for the dispatching strategy are presented (**Section 2.5**): power block full-load operation and load curve-based operation. Finally, indicators characterizing the CSP plant, especially the Levelized Cost of Electricity, are introduced (**Section 2.6**). When not specified, the methodology considers a single solar field array and can be applied to any of the layout configurations detailed in **Section 3.1**.

2.1. **HALOS**

Heliostat Aimpoint and Layout Optimization Software (HALOS) is an open-source decision tool developed by the National Renewable Energy Laboratory (NREL) and implemented Python [47]. It employs mixed-integer programming models to determine the optimal aimpoint strategy for the solar field in CSP central receiver plants. HALOS considers various input parameters such as weather conditions, location details, heliostat specifications, solar field layout, and receiver characteristics, and generates an aiming strategy that maximizes thermal power delivery to the receiver while adhering to constraints on the thermal flux profile. Additionally, HALOS includes a module that interfaces directly with SolarPILOT, an NREL-developed tool for characterizing solar field performance and generating layouts and flux maps that serve as input to the models [48].

2.1.1. Model Formulation and Description

To reduce the computational effort of flux maps generations, two approximations are introduced:

- 1. Receiver surface discretization. The receiver surface is discretized into two grids. The first grid consists of measurement points, aiding in estimating thermal power delivery and ensuring adherence to flux constraints. The second grid comprises aimpoints, which heliostats may target.
- 2. Flux maps translation without recalculation. A flux map is initially calculated when a central aimpoint is selected, considering a specific heliostat and sun location. For each other aimpoint, the central flux map is shifted by the distance between the aimpoint itself and the central one, eliminating the need for recalculation.

In **Table 4** the notation used in the optimization model formulation is reported.

Table 4: HALOS Notation

Stets and Inc	lices	
$h \in \mathcal{H}$:	heliostats	
$m \in \mathcal{M}$:	receiver measurement points	
$m \in \hat{\mathcal{M}}_m$:	measurement points that neighbor measurement point m	
$a \in \mathcal{A}$:	receiver aimpoints	
Parameters		Units
C_{hma} :	thermal flux incident to measurement point m when heliostat h aims at point a on the receiver	$[\mathrm{W/m}^2]$
S_m :	surface area allocated to measurement point m	$[m^2]$
B_m :	upper limit on thermal flux incident to measurement point m	$[\mathrm{W/m}^2]$
$D_{mm'}$:	upper limit on difference in flux incident to measurement points m and m '	$[\mathrm{W/m^2}]$
Decision Vari	iables	Units
y_{ha} :	1 if heliostat h focuses on aimpoint a , and 0 otherwise	[-]
x_m :	thermal flux delivered to measurement point m	$[W/m^2]$

In a general form, the optimization model can be formulated as follows.

$$z^* = \max\left(\sum_{m \in \mathcal{M}} S_m \cdot x_m\right)$$

$$x_m = \sum_{h \in \mathcal{H}} \sum_{a \in \mathcal{A}} C_{hma} \cdot y_{ha} \quad \forall m \in \mathcal{M}$$
(6)

$$x_m = \sum_{h \in \mathcal{H}} \sum_{a \in \mathcal{A}} C_{hma} \cdot y_{ha} \quad \forall m \in \mathcal{M}$$
 (6)

$$x_m \le B_m \quad \forall m \in \mathcal{M} \tag{7}$$

$$x_m - x_{m'} \le D_{mm'} \quad \forall (m, m') \in \mathcal{M} \times \mathcal{M}$$
 (8)

$$x_m \ge 0 \quad \forall m \in \mathcal{M} \tag{9}$$

$$y_{ha} \in \{0,1\} \quad \forall h \in \mathcal{H}, a \in \mathcal{A}$$
 (10)

Equation 5 defines the objective function, which aims to determine the coupling of heliostats and aimpoints to maximize power collection on the receiver surface. The collected power is calculated as the sum of the thermal flux delivered to each measurement point multiplied by the allocated area. Constraint 6 restricts the computation of thermal flux to only the selected aimpoints. Constraint 7 and Constraint 8 limit the incident flux on measurement points and the thermal gradient between two adjacent points, respectively. Lastly, Constraint 9 and Constraint 10 ensure that variables maintain realistic values.

To enhance computational efficiency, the optimization problem undergoes the following strategies:

- 1. Spatial Decomposition. The solar field is partitioned into sections for which the aimpoints are optimized in parallel, by introducing constraints on allowable flux limits for each section. Subsection solutions are then aggregated and adjusted to derive the overall strategy.
- 2. Heuristic Grouping Method. The solar field is divided into heliostats groups, whose size is pre-specified. Each group of heliostats is directed towards the same aimpoints on the receiver. This approach reduces the model size by a factor corresponding to the group size.

HALOS Functioning and Problems

The schematic shown in Figure 2 briefly summarizes how HALOS works. For the purpose of this research, the solar field layout is predetermined and central flux maps are generated using SolarPILOT.

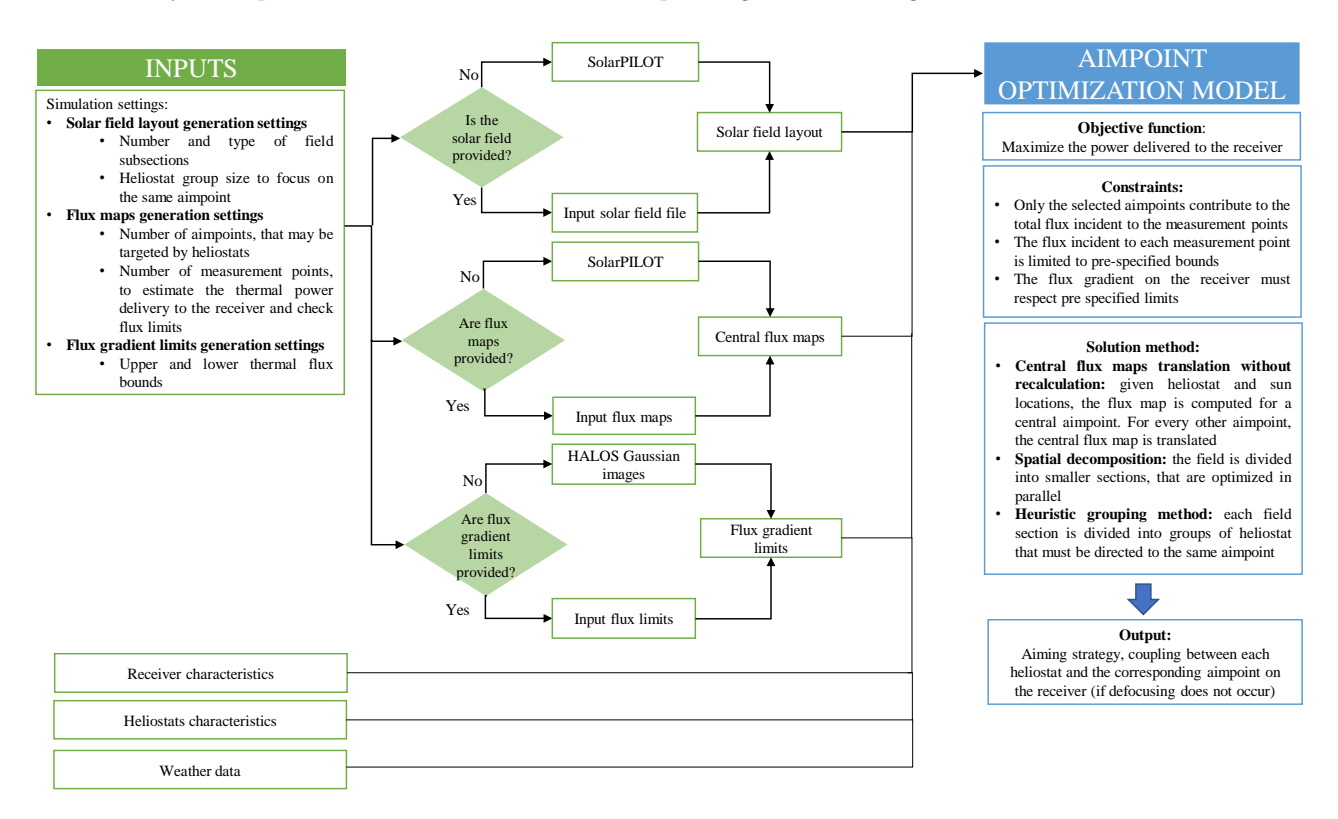


Figure 2: HALOS flowchart

HALOS generates thermal flux maps on the receiver surface based on the given heliostats and sun positions, combining the input central flux maps and considering the optimal heliostat-aimpoint associations. HALOS also provides aimpoints coordinates, heliostat-aimpoint associations, and identifies defocused heliostats within the solar field. It is feasible to set HALOS aimpoints coordinates into SolarPILOT and assess the extent to which the resulting flux maps align with those generated by HALOS. The first challenge encountered involves aligning the two reference systems.

On a cylindrical receiver, HALOS utilizes vertically-shifted aimpoints with respect to the receiver equatorial line. Each heliostat aims at the origin of the reference system and can choose from a set of aimpoints along the vertical direction. Visualizing the solar field from above, is it possible to envision a ray connecting the heliostat center to the receiver center. The intersection with the receiver surface pinpoints the position of the aimpoints column (refer to **Figure 3(a)**). For each heliostat, HALOS provides the vertical displacement of the corresponding aimpoint with respect to the receiver equatorial line, $Z_{\rm H}$. The associated SolarPILOT coordinates require the computation of angle α , where $X_{\rm He}$ and $Y_{\rm He}$ represent the heliostat position coordinates in the field.

$$\alpha = \arctan\left(\frac{X_{\text{He}}}{Y_{\text{He}}}\right) \tag{11}$$

SolarPILOT x- and y-coordinates are represented by the components of a rotating vector originating from the centre of the reference system and directed towards the receiver surface. They are computed, together with the z-coordinate, as shown in **Equations 12**, where r_{rec} is the receiver radius and h_{tower} is the receiver tower optical height.

$$\begin{cases} X_{\rm SP} = r_{\rm rec} \cdot \sin \alpha \\ Y_{\rm SP} = r_{\rm rec} \cdot \cos \alpha \\ Z_{\rm SP} = Z_{\rm H} + h_{\rm tower} \end{cases}$$
 (12)

On a flat plate receiver, HALOS utilizes a two-dimensional grid of aimpoints. In its reference system, each aimpoint is characterized by three coordinates (refer to **Figure 3(b)**). $X_{\rm H}$ is the horizontal displacement of the aimpoint with respect to the centre of the flat plate. $Y_{\rm H}$ is the angle between the aimpoint position on the flat plate and the vertical direction. $Z_{\rm H}$ is the optical height of the aimpoint. The conversion of these coordinates into SolarPILOT reference system is shown in **Equations 13**.

$$\begin{cases}
X_{\text{SP}} = -X_{\text{H}} \\
Y_{\text{SP}} = Y_{\text{H}} \\
Z_{\text{SP}} = Z_{\text{H}}
\end{cases}$$
(13)

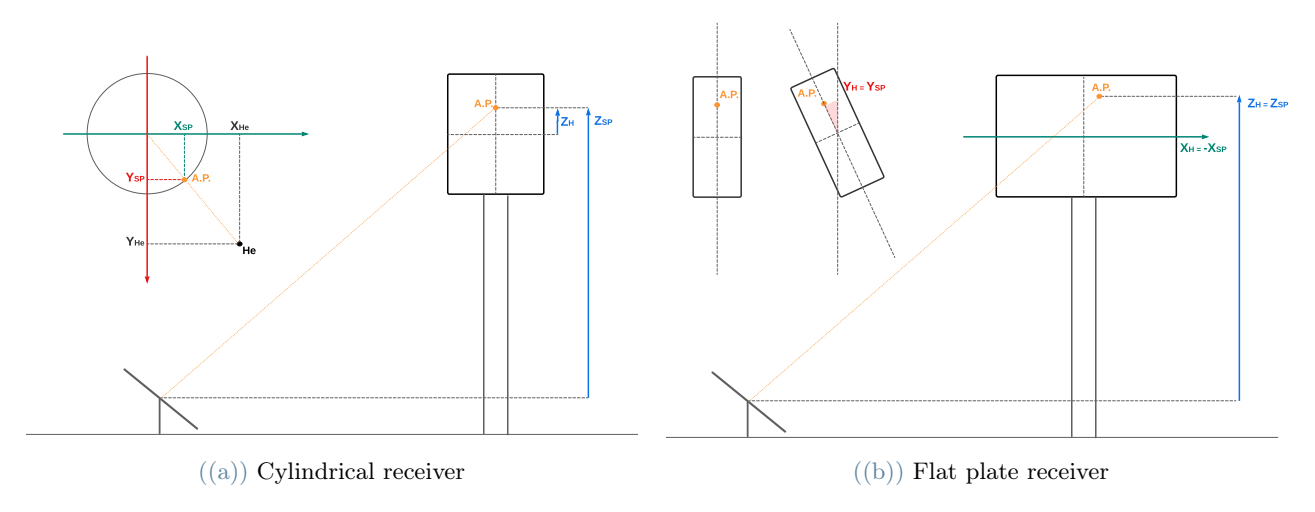


Figure 3: HALOS and SolarPILOT reference systems

While the conversion between the two reference systems appears to be effective for the case studies analyzed by the developers, inconsistencies arise when applied to larger solar fields. As an example, HALOS is executed for the base case study detailed in **Section 3**, and the resulting aimpoints are used as input to SolarPILOT. The respective flux maps are illustrated in **Figure 4(a)** and **Figure 4(b)**, for midday on the 8th of January. The flux distributions exhibit different shapes, and SolarPILOT's flux map exceeds the peak flux limit of $1000 \, \text{kW/m}^2$.

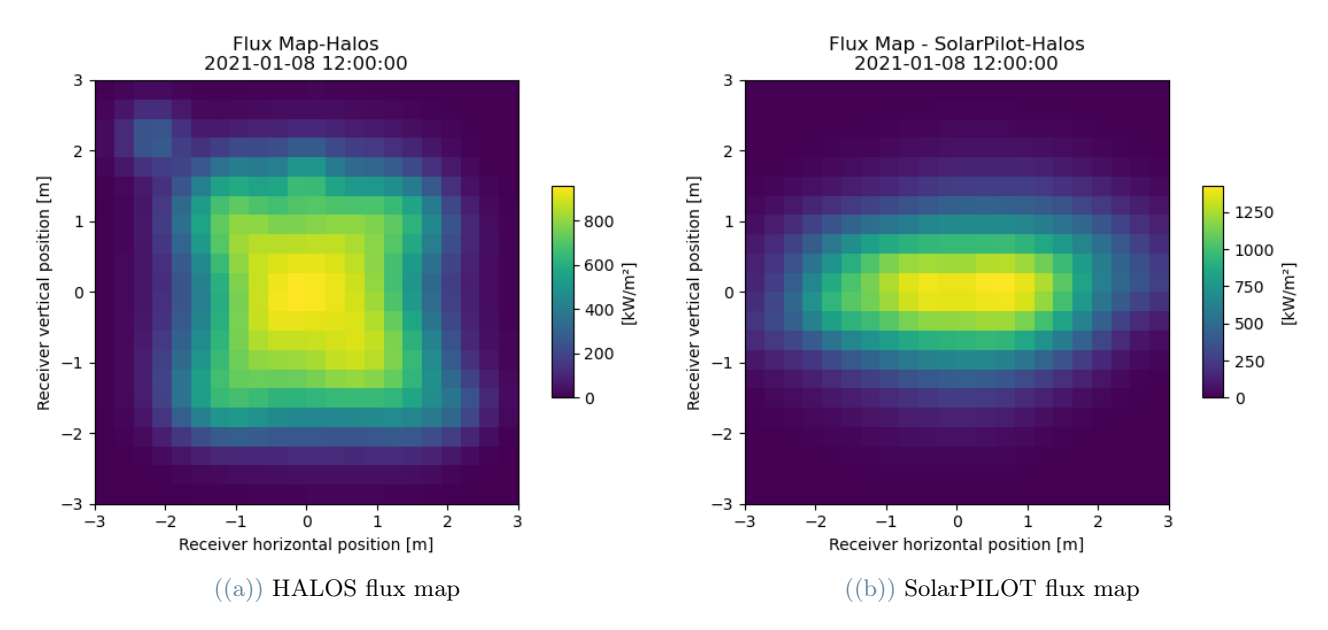


Figure 4: Flux maps comparison

Numerous attempts have been made to rectify the mismatch between the tools, but a consistent resolution has not been achieved yet. Consequently, HALOS is deemed unsuitable for the purposes of this research and is abandoned. The NREL is actively addressing these issues with the potential for future software use.

2.2. SolarPILOT and Heuristic Defocusing

Solar Power Tower Integrated Layout and Optimization Tool (SolarPILOT) is a tool developed by the NREL for designing, characterizing, and optimizing CSP tower plants [48]. It uses an analytical simulation engine based on a modified Gaussian series expansion to characterize the image generated by each heliostat. Unlike ray-tracing-based tools, that construct the model using numerous rays and probabilistic modeling to achieve a Gaussian-form image, SolarPILOT incorporates error distributions directly into its analytical formulation. This explicit modeling approach enables faster solving.

SolarPILOT facilitates optical and thermal performance simulations based on the specifications of the receiver and heliostats, solar field characteristics, and weather data. The flux analytical Hermite polynomial simulation model is employed in this application. The simulation produces flux maps, and the choice of the aiming strategy influences the results. Among the available built-in options, *Image Size Priority* aiming method is relevant to the objectives of this research, as it allows for the dispersion of the thermal flux across the receiver surface rather than concentrating it in a narrow region. This method determines heliostats aimpoints positions by sequentially placing them on the receiver at locations with the lowest flux. The order of placement is influenced by the size of the image on the receiver, prioritizing images with notable distortion or those situated at a greater distance. Following each heliostat placement, SolarPILOT identifies a local minimum in flux intensity and adjusts the position of the next heliostat accordingly.

Image Size Priority aiming method offers the advantage of distributing thermal flux across the receiver surface, thereby minimizing the flux gradient. However, the design constraints impose limits on the maximum power that can be collected on the receiver. SolarPILOT lacks an engine capable of detecting over-fluxes and subsequently defocusing heliostats, making necessary the development of a custom Heuristic defocusing strategy, which is depicted in the flowchart presented in **Figure 5**.

The algorithm is implemented in Python, accessing the functionalities of SolarPILOT via the Co-Pylot API (Application Programming Interface) [47]. This allows for the simulation of solar field performance on an hourly basis. The inputs are those required by SolarPILOT, plus the cleanliness time series, that will be discussed in Section 2.3. The solar field is operated when the sun elevation angle is higher than the stow angle. When this condition is met, $Image\ Size\ Priority$ aiming strategy is run, given the cleanliness loss at the current time step and the defocusing strategy at the previous time step. The resulting total power incident on the receiver may exceed the design value, $Q^{\rm threshold}$. To address this issue, heuristic defocusing and re-focusing strategies are formulated. The following variables are defined:

• Q^{in} is the total power incident on the receiver, as provided by SolarPILOT, applying the defocusing strategy of the previous time step. It does not necessarily respect the threshold.

• Q^{fin} is the total power incident on the receiver, after defocusing or re-focusing. It always complies with the threshold.

When $Q^{\rm in}$ exceeds the threshold, defocusing takes place. The solar field is divided into eight radial sectors: to evenly distribute the defocused heliostats, eight heliostats are defocused simultaneously, one for each sector. The defocusing process starts from the heliostats closer to the receiver, the most efficient ones, to speed up the computation. Defocusing ceases when the power incident on the receiver, $Q^{\rm fin}$, falls below the threshold. On the other hand, when $Q^{\rm in}$ is smaller than $Q^{\rm threshold}$, there is potential for refocusing. Firstly, an attempt is made to refocus all the defocused heliostats. If the resulting $Q^{\rm fin}$ complies with the threshold, refocusing is promptly executed. Otherwise, heliostats are refocused in groups of four, following the defocusing order, until the threshold is met. In general, $Q^{\rm fin}$ is close but never equal to $Q^{\rm threshold}$, due to the problem discretization.

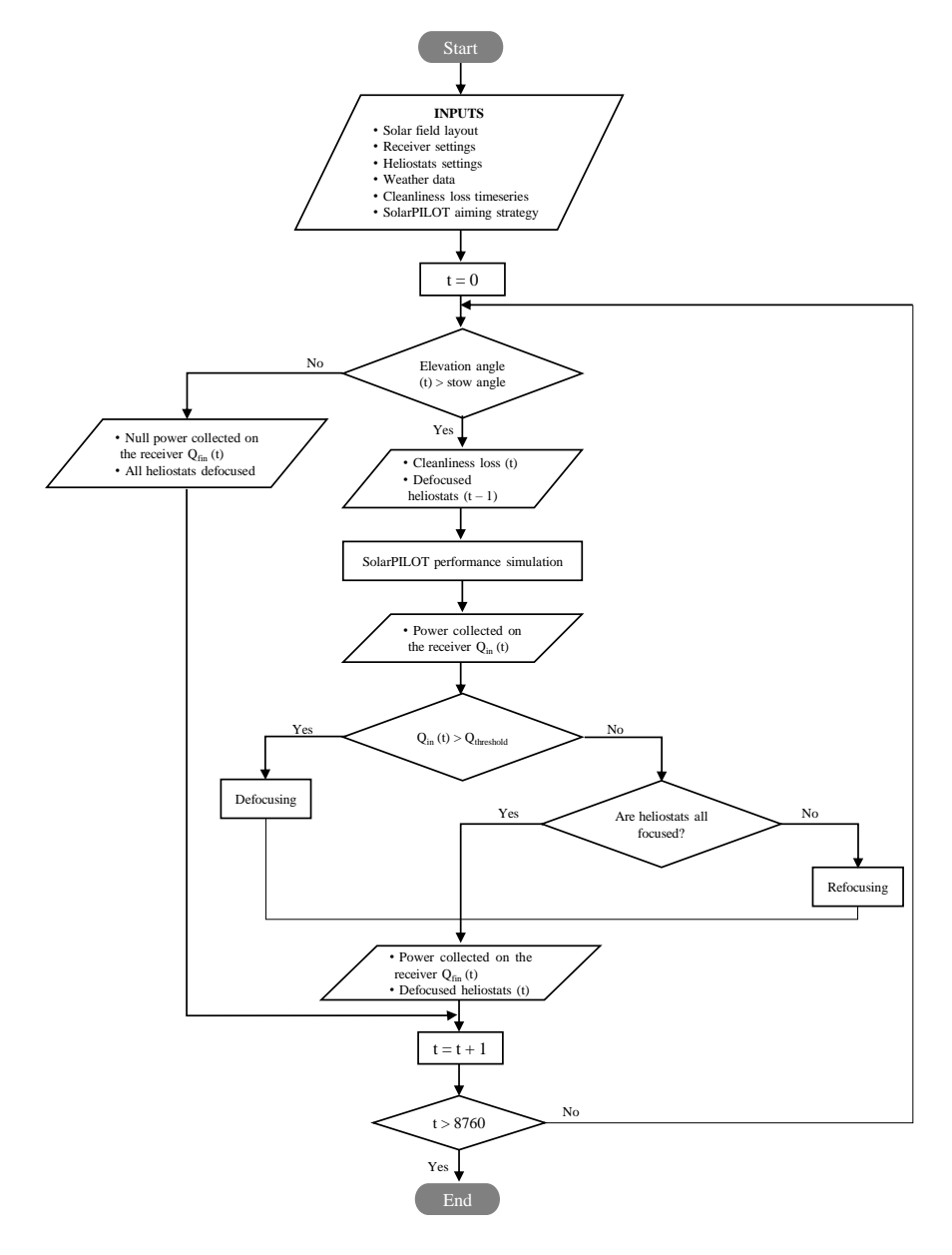


Figure 5: Heuristic defocusing strategy flowchart

The solar field is partitioned into eight sectors based on heliostats' polar angles, following the methodology proposed by HALOS [47]. For each heliostat with coordinates $(X_{\rm He}, Y_{\rm He})$, the corresponding polar angle θ is computed using the distance d between the heliostats and the origin of the reference system.

$$d = \sqrt{X_{\rm He}^2 + Y_{\rm He}^2} \tag{14}$$

The polar angle is considered positive if measured clockwise and is calculated as per Equation 15.

$$\theta = \begin{cases} \arccos\left(\frac{X_{\text{He}}}{d}\right) & Y_{\text{He}} \ge 0\\ 2\pi - \arccos\left(\frac{X_{\text{He}}}{d}\right) & Y_{\text{He}} < 0 \end{cases}$$
 (15)

Heliostats are arranged based on their polar angles relative to due east. Once sorted, heliostats are assigned to sections in such a way that each section contains approximately an equal number of heliostats.

2.3. Soiling Model and Cleaning Strategy

Soiling predictions and cleaning strategy optimization are based on the work by Anderson et al. (2023) [44].

2.3.1. Soiling Losses Prediction

In accordance with the Dry-Deposition Soiling Model delineated by Picotti et al. (2018) [36], the cumulative number of dust particles falling on the heliostat at time t is shown by **Equation 16**. D is the spherical particle diameter and $n_i(D)$ is the deposition rate during the sampling period Δt of meteorological measurements.

$$N_t(D) = \sum_{i=1}^t n_i(D) \cdot \Delta t \tag{16}$$

The reflective area loss due to soiling is computed incorporating $a(\theta_t, D)$, the area lost for a particle of diameter D and at incidence angle θ_t .

$$A_t^{\text{loss}}(\theta_t) = \int_0^\infty N_t(D) \cdot a(\theta_t, D) dD$$
(17)

Under the assumption of well-separated particles on the surface, the area lost encompasses shaded and blocked regions of the reflector while subtracting the overlapping area.

$$a(\theta_t, D) = A^{\text{shade}}(\theta_t, D) + A^{\text{block}}(\theta_t, D) - A^{\text{overlap}}(\theta_t, D) = 2 \cdot \frac{\pi D^2}{4 \cos \theta_t} - A^{\text{overlap}}(\theta_t, D)$$
(18)

As the incidence angle approaches zero, the area loss simplifies to $a(\theta, D) = \frac{\pi D^2}{4}$, representing the cross-sectional area of the dust particle. A geometry factor g is defined as the ratio between the generic reflective area loss and that with normal incidence angle. If no overlap is assumed, g is expressed as per **Equation 19**.

$$g = a(\theta_t, D) \cdot \frac{4}{\pi D^2} = \frac{\pi D^2}{2\cos\theta_t} \cdot \frac{4}{\pi D^2} = \frac{2}{\cos\theta_t}$$
 (19)

This approximation can be adopted for particles below $100\,\mu\mathrm{m}$ and incidence angles above 1. The area loss can be approximated through the geometry factor, where A_t^{norm} is the total area loss with normal incidence angle.

$$A_{t}^{\text{loss}}\left(\theta_{t}\right) = \int_{0}^{\infty} N_{t}\left(D\right) \cdot g \cdot \frac{\pi D^{2}}{4} dD = \frac{2}{\cos\theta_{t}} \cdot \left[\frac{\pi}{4} \int_{0}^{\infty} D^{2} \cdot N_{r}\left(D\right) dD\right] = \frac{2}{\cos\theta_{t}} \cdot A_{t}^{\text{norm}} \tag{20}$$

The reflectance is computed according to **Equation 21**, where A^{mirror} is the mirror reflective area and ρ_0 is the as-clean reflectance.

$$\hat{\rho}_t(\theta_t) = \rho_0 \left(1 - \frac{A_t^{\text{loss}}}{A^{\text{mirror}}} \right) = \rho_0 \left(1 - \frac{2}{\cos \theta_t} \frac{A_t^{\text{norm}}}{A^{\text{mirror}}} \right)$$
(21)

Finally, the surface roughness ratio h_r/z_0 of the Dry-Deposition Soiling Model is estimated using a least means squared fit between measured and predicted reflectance values. The Dry-Deposition Soiling Model is then employed to predict soiling rates for a solar field, based on meteorological data and solar field design conditions.

2.3.2. Cleaning Strategy Optimization

The tool employed to optimize the deployment of cleaning resources, named HelioSoil, is a cleaning heuristic operating on a fixed-frequency time base. This approach aims to strike a balance between the costs associated with cleaning the heliostat field and the productivity of the power plant. The solar field is divided into J sectors, each represented by a representative heliostat. Within each sector, all heliostats are assumed to have the same soiled area and incidence angle. The parameter R denotes the number of sectors that can be cleaned by M cleaning crews in one day, leading to F full-field cleans per year. The value of R depends on the chosen technology and the size of the cleaning crew. The optimal values for M and F are computed by minimizing the total cleaning cost.

$$TCC(M, F) = C^{cl} + C^{deg}$$
(22)

The direct cleaning cost C^{cl} account for the cost of the cleaning truck C^{truck} with a lifetime of b years, operator salaries C^{salary} , maintenance costs C^{maintain} , and water and fuel expenses $C^{\text{w\&f}}$. A_j^{total} represents the total heliostat area of the j-th sector.

$$C^{\text{cl}}(M, F) = \left(\frac{C^{\text{truck}}}{b} + C^{\text{salary}} + C^{\text{mantain}}\right)M + \sum_{j=1}^{J} C^{\text{w&f}} \cdot A_j^{\text{total}} \cdot F$$
(23)

The degradation cost C^{deg} accounts for the difference in revenues between pristine field conditions and those affected by soiling and the adopted cleaning schedule. P is electricity sale price, $C^{\text{O\&M}}$ is the price of O&M costs unrelated to cleaning, w_t^{clean} and w_t^{soil} are the electrical powers generated from a clean solar field and form a soiled one, respectively.

$$C^{\text{deg}}(M, F) = \left(P - C^{\text{O&M}}\right) \sum_{t=1}^{T} \left(w_t^{\text{clean}} - w_t^{\text{soil}}\right) \Delta t \tag{24}$$

The cleaning strategy optimization is based on the following assumptions:

- Optical efficiencies are obtained interpolating the values in a lookup table, built simulating the solar field performance with SolarPILOT *Image Size Priority* aiming strategy for discrete solar angles.
- Continuous dispatch policy is assumed, without considering thermal energy storage.
- The cost metrics is fixed for all the solar field configurations.
- The economic parameters are those stated by Anderson et al. [44], adjusting the cleaning speed for 7.5 hours-long shifts and converting them into USD.

The soiling rate of each mirror is updated for each time step. $N_{t,j}$ and $N_{t+1,j}$ represent the cumulative number of particles before and after the cleaning event, respectively. $\eta_{cl} \in [0,1]$ is the cleaning efficiency and \mathcal{D} is the cleaning decision given for the considered cleaning schedule.

$$N_{t+1,j} = \begin{cases} n_{t,j}(D) + N_{t,j}(D)(1 - \eta_{cl}(D)) & \mathcal{D}_{t+1,j} = 1\\ n_{t,j}(D) + N_{t,j}(D) & \mathcal{D}_{t+1,j} = 0 \end{cases}$$
(25)

2.4. Drivers Failure

Drivers failure problem is a Markov decision process, whose schematic is shown in **Figure 6**. In the picture, N represents the number of heliostats, λ the failure rate, and $\mathcal{R}\mu$ the repair rate. The analysis operates under the following assumptions:

- Heliostats are treated as identical assets, sharing the same efficiency.
- Failure rates are assumed to be constant over time, with no consideration for aging effects.
- Repair rates are considered constant: the number of repair crews R is constant and the n crews working on a single heliostat can repair it n times faster.
- The steady-state analysis indicates how many heliostats are down but does not identify which specific heliostats have failed.
- The steady-state analysis is pessimistic, as steady state is achieved after an extended period. This implies that the distribution will show more heliostats down in the initial years than it should actually be.

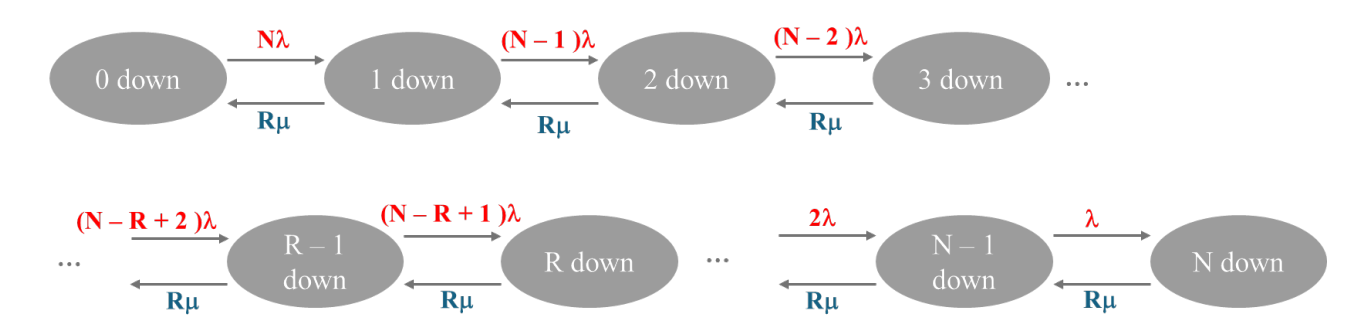


Figure 6: Markov decision process

Given the number of heliostats in the solar field, the heliostats failure rate, the repair rate, and the number or workers, the steady-state probability distribution of the number of heliostats subjected to failure, p_{ss} , is computed. The availability target, \bar{A}_{hel} , and the repair rate are set, and the number of workers is tuned

accordingly. The resulting steady-state probability distribution allows for the computation of the number of heliostats that are down in steady state, $n_{\rm hel,down}$. The reliability analysis is conducted for the entire plant, thus considering the heliostats arrays all together.

$$n_{\text{hel,down}} = n_{\text{hel}} \cdot (1 - \bar{A}_{\text{hel}}) \tag{26}$$

Together with the reliability analysis, an economic analysis is undertaken because failures affect both the energy collected on the receiver surface and O&M costs. Firstly, the power collected on the receiver Q^{fin} , as obtained from the algorithm described in **Section 2.2**, must be penalized. If defocusing does not occur, the power incident on the receiver is reduced by a factor equal to the availability target, as per **Equation 27**. If defocusing occurs, it is assumed that the first heliostats to be defocused are those subjected to failure. The actual availability is computed as shown in **Equation 28**, and the power is penalized as before.

$$Q_t^{\text{rec}} = \bar{A}_{\text{hel}} \cdot Q_t^{\text{fin}} \tag{27}$$

$$A_{\text{hel}} = \frac{n_{\text{hel}} - (n_{\text{hel,down}} - n_{\text{hel,defocused}})}{n_{\text{hel}}}$$
(28)

Secondly, the O&M costs are increased due to the necessity of repairing the broken drivers. The repair cost rate can be computed given the probability $p_{\rm ss,0}$ of having no heliostats down, the average cost to fix one failure $C_{\rm failure}$ accounting for both labour and materials, and the number of operating hours $H_{\rm op}$.

$$C_{\text{repair}} = C_{\text{failure}} \cdot (1 - p_{\text{ss},0}) \cdot \mathcal{R}\mu \cdot H_{\text{op}}$$
 (29)

$$C_{\text{failure}} = C_{\text{worker}} \cdot \frac{n_{\text{workers}}}{\mathcal{R}\mu} + C_{\text{p\&t}}$$
 (30)

The reliability and economic analysis assumptions are shown in **Table 5** and **Table 6**. The failure rate is defined based on SolarOne power plant data [45], while workers salaries and material costs are based on SolarTwo power plant data [49] accounting for inflation.

Table 5: Reliability analysis assumptions

Table 6: Economic analysis assumptions

Parameter		Value	Parameter		Value
Availability	$ar{A}_{ m hel}$	97%	Worker salary	C_{worker}	40 USD/hour/worker
Failure rate	λ	6.13×10^{-5} failure/hour	Parts and tools	$C_{\rm p\&t}$	$230\mathrm{USD/repair}$
Repair rate	$\mathcal{R}\mu$	1 repairs/hour/worker	Operating hours	H_{op}	3828 hours/year

2.5. Dispatching strategy and Thermal Energy Storage

As a result of the steps described in the previous sections, the power collected on the receiver surface, $Q^{\rm rec}$, is obtained for each time step for the single solar field array. The power absorbed by the HTF accounts for receiver absorbance and for thermal losses, including convective, radiative, and piping losses. For the single solar field array, $Q^{\rm HTF,\ array}$ is computed considering a constant thermal power loss, $Q^{\rm loss}$.

Following the algorithm outlined in **Section 2.2** ensures that Q^{rec} complies with receiver saturation conditions and does not exceed $Q^{\text{threshold}}$. Further validation is required regarding receiver deprivation conditions (refer to **Equations 31**): if the power incident on the receiver is less than the thermal losses, the receiver is deactivated, and the power absorbed by the HTF is set to zero.

$$Q_t^{\text{HTF, array}} = \begin{cases} Q_t^{\text{rec}} - Q^{\text{loss}} & Q_t^{\text{rec}} > Q^{\text{loss}} \\ 0 & Q_t^{\text{rec}} \le Q^{\text{loss}} \end{cases}$$
(31)

From this point onward, as the dispatching strategy and TES come into consideration, the focus shifts to the entire plant rather than an individual solar field array. The total power absorbed by the HTF is calculated considering the total number of solar field arrays $n_{\rm array}$.

$$Q_t^{\rm HTF} = Q_t^{\rm HTF, \, array} \cdot n_{\rm array} \tag{32}$$

Given the power block power rated power P_{CSP} , the rated thermal power to drive the turbine at full load, $Q^{\text{HTF, PB, max}}$, and the TES capacity, $E^{\text{TES, max}}$, are computed. η_{PB} is the power block efficiency and h_{TES}

represents the thermal energy storage hours.

$$Q^{\text{HTF, PB, max}} = \frac{P_{\text{CSP}}}{\eta_{\text{PB}}}$$

$$E^{\text{TES, max}} = Q^{\text{HTF, PB, max}} \cdot h_{\text{TES}}$$
(33)

$$E^{\text{TES, max}} = Q^{\text{HTF, PB, max}} \cdot h_{\text{TES}}$$
 (34)

The power absorbed by the HTF can be directed either to the power block $(Q^{\text{HTF, PB}})$ or to the TES $(Q^{\text{HTF, TES}})$. In cases where both are saturated, any excess power is dissipated ($Q^{HTF,diss}$). The yearly electricity production and energy dissipation can be computed as shown in Equation 35 and Equation 36 respectively.

$$EE = \sum_{t=1}^{8760} Q_t^{\text{HTF, PB}} \cdot \eta_{\text{PB}}$$
 (35)

$$E^{\text{diss}} = \sum_{t=1}^{8760} Q_t^{\text{HTF, diss}}$$
 (36)

Two dispatching options are available and discussed in the following sections.

2.5.1.**Full Load Operation**

The power plant is operated prioritizing full-load operation of the turbine: if the receivers thermal power output is not enough, the missing thermal energy is taken from the TES, if available. If such thermal output exceeds the maximum thermal power to be sent to the power block, the excess heat is sent to the TES, if there is available capacity. Finally, if the storage is full, the excess heat is dissipated. The total power absorbed by the HTF is compared with the maximum power to be sent to the power block and four dispatching options are defined. Several thermal energy storage hours, ranging from 0 h to $h_{\rm max}$, are considered. $h_{\rm max}$ corresponds to the maximum TES size explored, leading to null yearly thermal energy dissipation.

Option 1. If $Q_t^{\text{HTF}} < Q^{\text{HTF, PB, max}}$ and $E_{t-1}^{\text{TES}} - \left(Q^{\text{HTF, PB, max}} - Q_t^{\text{HTF}}\right) \cdot \Delta t \ge 0$:

$$\begin{cases} Q_t^{\text{HTF, PB}} = Q^{\text{HTF, PB, max}} \\ Q_t^{\text{HTF, TES}} = -\left(Q^{\text{HTF, PB, max}} - Q_t^{\text{HTF}}\right) \\ Q_t^{\text{HTF, diss}} = 0 \\ E_t^{\text{TES}} = E_{t-1}^{\text{TES}} + Q_t^{\text{HTF, TES}} \cdot \Delta t \end{cases}$$

$$(37)$$

Option 2. If $Q_t^{\text{HTF}} < Q^{\text{HTF, PB, max}}$ and $E_{t-1}^{\text{TES}} - \left(Q^{\text{HTF, PB, max}} - Q_t^{\text{HTF}}\right) \cdot \Delta t < 0$:

$$\begin{cases} Q_t^{\text{HTF, PB}} = Q_t^{\text{HTF}} + \frac{E_{t-1}^{\text{TES}}}{\Delta t} \\ Q_t^{\text{HTF, TES}} = -\frac{E_{t-1}^{\text{TES}}}{\Delta t} \\ Q_t^{\text{HTF, diss}} = 0 \\ E_t^{\text{TES}} = 0 \end{cases}$$
(38)

Option 3. If $Q_t^{\text{HTF}} \geq Q^{\text{HTF, PB, max}}$ and $E_{t-1}^{\text{TES}} + \left[Q_t^{\text{HTF}} - Q^{\text{HTF, PB, max}}\right] \cdot \Delta t \geq E^{\text{TES, max}}$:

$$\begin{cases} Q_t^{\text{HTF, PB}} = Q^{\text{HTF, PB, max}} \\ Q_t^{\text{HTF, TES}} = \frac{E^{\text{TES, max}} - E_{t-1}^{\text{TES}}}{\Delta t} \\ Q_t^{\text{HTF, diss}} = Q_t^{\text{HTF}} - Q_t^{\text{HTF, PB}} - Q_t^{\text{HTF, TES}} \\ E_t^{\text{TES}} = E^{\text{TES, max}} \end{cases}$$
(39)

 $\textbf{Option 4.} \ \ \text{If} \ Q_t^{\text{HTF}} \geq Q^{\text{HTF, PB, max}} \ \ \text{and} \ \ E_{t-1}^{\text{TES}} + \left[Q_t^{\text{HTF}} - Q^{\text{HTF, PB, max}}\right] \cdot \Delta t < E^{\text{TES, max}}.$

$$\begin{cases} Q_t^{\text{HTF, PB}} = Q^{\text{HTF, PB, max}} \\ Q_t^{\text{HTF, TES}} = Q_t^{\text{HTF}} - Q^{\text{HTF, PB, max}} \\ Q_t^{\text{HTF, diss}} = 0 \\ E_t^{\text{TES}} = E_{t-1}^{\text{TES}} + Q_t^{\text{HTF, TES}} \cdot \Delta t \end{cases}$$

$$(40)$$

2.5.2. Load-Based Operation

The power plant is operated with the goal of matching a pre-specified load curve. For each time step, the load curve provides the power to be produced by the plant, $P_{\rm des}$, corresponding to a HTF thermal power of $Q_{\rm HTF,des}$. If the HTF thermal power exceeds the request by the power block, the excess is sent to the TES or dissipated, depending on the available capacity. If the HTF thermal power is not enough, the missing thermal energy is taken from the TES. If the TES energy is not enough, part of the load, $P_{\rm uns}$, is not satisfied. The total power absorbed by the HTF is compared to the thermal power required by the power block and four dispatching options are defined. Several thermal energy storage hours, ranging from 0 h to $h_{\rm max}$, are considered. $h_{\rm max}$ corresponds to the maximum TES size explored, allowing to fully satisfy the load curve.

The load curve to be followed by the CSP plant is obtained gathering hourly electricity production data from the Australian Energy Market Operator (AEMO) and categorizing them by source, distinguishing between renewables-based and combustion-based sources (refer to **Figure 7(a)**). The residual load curve represents the electricity production that must still be met by renewables and is determined by subtracting the electricity generated by combustion-based plants from the total production. It is subsequently normalized and scaled with respect to the nominal capacity of the CSP plant (refer to **Figure 7(b)**).

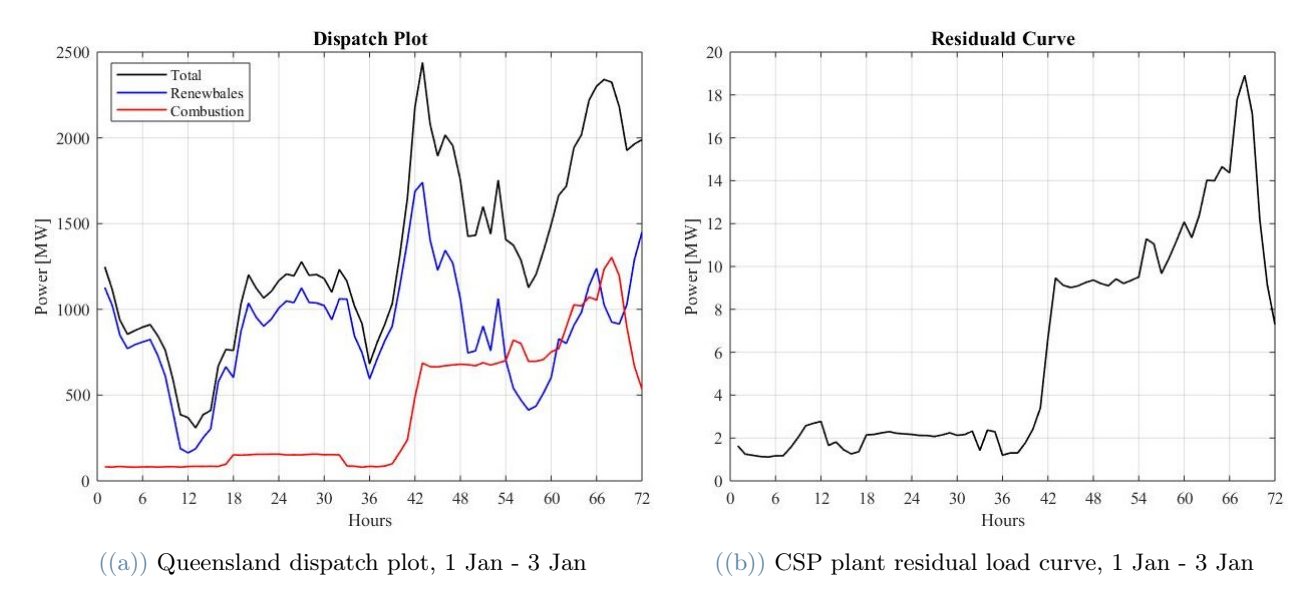


Figure 7: Queensland dispatch plot and residual load curve

$$\begin{aligned} \textbf{Option 1.} & \text{ If } Q_t^{\text{HTF, PB, des}} = Q_t^{\text{HTF, PB, des}} - Q_t^{\text{HTF, PB, des}} - Q_t^{\text{HTF}} \Big) \cdot \Delta t \geq 0; \\ & \begin{cases} Q_t^{\text{HTF, PB}} = Q_t^{\text{HTF, PB, des}} \\ Q_t^{\text{HTF, TES}} = -\left(Q_t^{\text{HTF, PB, des}} - Q_t^{\text{HTF}}\right) \\ Q_t^{\text{HTF, diss}} = 0 \\ Q_t^{\text{HTF, diss}} = 0 \end{cases} \\ & \begin{cases} E_t^{\text{TES}} = E_{t-1}^{\text{TES}} + Q_t^{\text{HTF, TES}} \cdot \Delta t \\ P_t^{\text{uns}} = 0 \end{cases} \end{aligned}$$

$$\textbf{Option 2.} \ \ \text{If If} \ Q_t^{\text{HTF, PB, des}} \ \ \text{and} \ \ E_{t-1}^{\text{TES}} - \left(Q_t^{\text{HTF, PB, des}} - Q_t^{\text{HTF}}\right) \cdot \Delta t < 0 :$$

$$\begin{cases} Q_t^{\text{HTF, PB}} = Q_t^{\text{HTF}} + \frac{E_{t-1}^{\text{TES}}}{\Delta t} \\ Q_t^{\text{HTF, TES}} = -\frac{E_{t-1}^{\text{TES}}}{\Delta t} \\ Q_t^{\text{HTF, diss}} = 0 \\ E_t^{\text{TES}} = 0 \\ P_t^{\text{uns}} = \left(Q_t^{\text{HTF, PB, des}} - Q_t^{\text{HTF, PB}}\right) \cdot \eta_{\text{PB}} \end{cases}$$

$$(42)$$

 $\textbf{Option 3.} \ \, \text{If} \, \, Q_t^{\text{HTF}} \geq Q_t^{\text{HTF, PB, des}} \, \, \text{and} \, \, E_{t-1}^{\text{TES}} + \left(Q_t^{\text{HTF}} - Q_t^{\text{HTF, PB, des}}\right) \cdot \Delta t \geq E^{\text{TES, max}}.$

$$\begin{cases} Q_t^{\text{HTF, PB}} = Q_t^{\text{HTF, PB, des}} \\ Q_t^{\text{HTF, TES}} = \frac{E^{\text{TES, max}} - E_{t-1}^{\text{TES}}}{\Delta t} \\ Q_t^{\text{HTF, diss}} = Q_t^{\text{HTF, Q}} - Q_t^{\text{HTF, PB}} - Q_t^{\text{HTF, TES}} \\ E_t^{\text{TES}} = E^{\text{TES, max}} \\ P_t^{\text{uns}} = 0 \end{cases}$$

$$(43)$$

 $\textbf{Option 4. If } Q_t^{\text{HTF}} \geq Q_t^{\text{HTF, PB, des}} \text{ and } E_{t-1}^{\text{TES}} + \left(Q_t^{\text{HTF}} - Q_t^{\text{HTF, PB, des}}\right) \cdot \Delta t < E^{\text{TES, max}};$

$$\begin{cases} Q_t^{\text{HTF, PB}} = Q_t^{\text{HTF, PB, des}} \\ Q_t^{\text{HTF, TES}} = Q_t^{\text{HTF}} - Q_t^{\text{HTF, PB, des}} \\ Q_t^{\text{HTF, diss}} = 0 \\ E_t^{\text{TES}} = E_{t-1}^{\text{TES}} + Q_t^{\text{HTF, TES}} \cdot \Delta t \\ P_t^{\text{uns}} = 0 \end{cases}$$

$$(44)$$

2.6. Indicators

Given a solar field layout, for each TES coupling, the following indicators are computed.

Energy loss due to defocusing and dissipation. The defocusing energy loss is defined as the ratio between the yearly energy loss due to heliostats defocusing, E^{def} , and the yearly energy that could be reflected on the receiver if all the heliostats were focused and no saturation constrain existed, E^{\max} (Equation 45). The dissipation energy loss is defined as the ratio between the yearly energy loss due to dissipation, $E^{\rm diss}$, and the yearly energy absorbed by the HTF, E^{HTF} (Equation 46). The total energy loss is given by the summation of these two contributions.

$$e^{\text{loss,def}} = \frac{E^{\text{def}}}{E^{\text{max}}} \cdot 100\%$$

$$e^{\text{loss,diss}} = \frac{E^{\text{diss}}}{E^{\text{HTF}}} \cdot 100\%$$
(45)

$$e^{\text{loss,diss}} = \frac{E^{\text{diss}}}{E^{\text{HTF}}} \cdot 100\% \tag{46}$$

Specific electricity production. The electricity production specific to the solar field area is defined as the ratio between the yearly electricity production, EE, and the area of the solar field $A_{\rm sf}$. It depends on the solar field size and coupled TES capacity, as well as on the adopted dispatching strategy.

$$EE_{\text{specific}} = \frac{EE}{A_{\text{sf}}}$$
 (47)

Levelized Cost of Electricity. The Levelized Cost of Electricity depends on the solar field size and TES capacity, as well as on the adopted dispatching strategy. CAPEX and OPEX, respectively capital expenditure and operating expense, will be detailed in the following sections. LT is the plant lifetime.

$$LCOE = \frac{\frac{CAPEX}{LT} + OPEX}{EE} \tag{48}$$

2.6.1. CAPEX

CAPEX is the capital expenditure to build the plant, characterized by direct and indirect costs, computed as indicated by System Advisor Model (SAM) [50]. The tower cost is obtained by exponentially scaling the fixed tower cost, $C_{\text{tower, fixed}}$, based on a scaling exponent k and the tower height h_{tower} .

$$C_{\text{tower, tot}} = \frac{1}{2} \cdot C_{\text{tower, fiexd}} \cdot e^{k \cdot h_{\text{tower}}}$$
 (49)

The receiver cost is determined by scaling the reference receiver cost, $C_{\text{receiver, ref}}$, using the ratio of the receiver area A_{rec} to the reference receiver area $A_{\text{rec, ref}}$, adjusted by the exponent k_{rec} .

$$C_{\text{receiver, tot}} = C_{\text{receiver, ref}} \cdot \left(\frac{A_{\text{rec}}}{A_{\text{rec, ref}}}\right)^{k_{\text{rec}}}$$
 (50)

The site improvement cost is computed by multiplying the specific cost of land improvement, $C_{\text{site, tot}}$, by the total solar field reflective area, A_{sf} . The heliostat field cost is calculated by multiplying the specific cost of the heliostat field, $C_{\text{heliostat}}$, by the total solar field reflective area, A_{sf} .

$$C_{\text{site, tot}} = C_{\text{site}} \cdot A_{\text{sf}}$$
 (51)

$$C_{\text{heliostat, tot}} = C_{\text{heliostat}} \cdot A_{\text{sf}}$$
 (52)

The balance of plant (BOP) cost is given by the specific cost, $C_{\text{BOP, ref}}$, multiplied by the power cycle rated power. The power cycle (PC) cost is given by the specific cost, $C_{\text{PC, ref}}$, times the power cycle rated power.

$$C_{\text{BOP}} = C_{\text{BOP, ref}} \cdot C_{\text{CSP}} \tag{53}$$

$$C_{\rm PC} = C_{\rm PC, ref} \cdot C_{\rm CSP}$$
 (54)

The TES cost is computed as the specific cost, C_{TES} , multiplied by the TES capacity, E_{TES} .

$$C_{\text{TES}} = C_{\text{TES, ref}} \cdot E_{\text{TES}}$$
 (55)

The contingency cost is given by the contingency rate, k_{cont} , times the Total Direct Cost (TDC). The TDC is computed for the entire CSP plant, considering all the heliostat arrays.

$$C_{\text{cont}} = k_{\text{cont}} \cdot \text{TDC}$$
 (56)

$$TDC = (C_{\text{tower, tot}} + C_{\text{receiver, tot}} + C_{\text{site, tot}} + C_{\text{heliostat}}) \cdot n_{\text{array}} + C_{\text{BOP}} + C_{\text{PC}} + C_{\text{TES}} + C_{\text{cont}}$$
 (57)

Land cost, sales tax cost, and EPC (engineering, procurement and construction) and owner costs contribute to the Total Indirect Cost (TIC). The land cost is determined by multiplying the reference land cost, $C_{\text{land, ref}}$, by the land area, A_{land} . The sales cost is obtained by multiplying the $r_{\text{sales, frac}}$ fraction of TDC and the land cost by the sales tax rate, r_{sales} . Finally, the EPC and owner costs are given by a fraction r_{EPC} of the TDC.

$$C_{\text{land, tot}} = C_{\text{land, ref}} \cdot A_{\text{land}}$$
 (58)

$$C_{\text{sales, tot}} = r_{\text{sales}} \cdot (\text{TDC} \cdot r_{\text{sales, frac}} + C_{\text{land, tot}})$$
 (59)

$$C_{\text{EPC}} = r_{\text{EPC}} \cdot \text{TDC}$$
 (60)

$$TIC = C_{land, \text{ tot}} + C_{sales, \text{ tot}}$$
(61)

In Table 7, the economic assumptions for CAPEX computation, as indicated by SAM [50], are summed up.

Table 7: CAPEX economic assumptions

Parameter		Value
Fixed tower cost	$C_{\mathrm{tower, fixed}}$	$3000000\mathrm{USD}$
Tower cost scaling exponent	k	0.00113
Receiver tower height	$h_{ m tower}$	52 m
Receiver reference cost	$C_{\text{receiver, ref}}$	$103000000\mathrm{USD}$
Receiver reference area	$A_{ m rec, ref}$	$1571\mathrm{m}^2$
Receiver cost scaling exponent	$k_{ m rec}$	0.7

Specific site improvement cost	$C_{ m site}$	$16\mathrm{USD/m^2}$
Specific heliostat field cost	$C_{ m heliostat}$	$66\mathrm{USD/m^2}$
Balance of plant specific cost	$C_{ m BOP, \ ref}$	$290\mathrm{USD/kWh_e}$
Power cycle specific cost	$C_{ m PC, \ ref}$	$1.040\mathrm{USD/kWh_e}$
TES specific cost	$C_{\mathrm{TES, ref}}$	$22\mathrm{USD/KWh_t}$
Contingency	$k_{ m cont}$	7 %
Specific land cost	$C_{\mathrm{land, ref}}$	$10.000\mathrm{USD/acre}$
Sales tax rate	$r_{ m sales}$	5 %
Sales tax rate portion	$r_{ m sales,\ frac}$	80 %
EPC portion	$r_{ m EPC}$	13 %

2.6.2. OPEX

OPEX is the operation and maintenance cost, and it is given by four contributions:

- Fixed cost by capacity, which depends on the CSP plant capacity (Equation 62).
- Variable cost by generation, which depends on the yearly electricity production (Equation 63).
- Cleaning cost, which depends on the adopted cleaning strategy and is computed and optimized as stated in **Section 2.3**. It accounted for only when considering soiled field conditions.
- Repair cost, which depends on the heliostat field availability and is computed as stated in **Section 2.4**.

$$OPEX_{fixed} = C_{fiexd, ref} \cdot P_{CSP}$$
 (62)

$$OPEX_{\text{variable}} = C_{\text{variable, ref}} \cdot EE_{\text{CSP}}$$
 (63)

The specific fixed and variable costs are computed as indicated by SAM, are shown in **Table 8**.

Table 8: OPEX economic assumptions

Parameter		Value
Fixed specific cost	$C_{ m fixed,ref}$	$66\mathrm{USD/kW/year}$
Variable specific cost	$C_{\text{variable,ref}}$	$3.5\mathrm{USD/MWh_e}$

3. Case study description

The North West Queensland Hybrid Power Project (NWQHPP) is a hybrid power plant situated in Mount Isa, Queensland, Australia. It features a CSP plant with a capacity of 56 MW. The facility is equipped with 30 modular solar fields, each consisting of 2389 heliostats. In **Table 9**, CSP plant characteristics are summarized.

Table 9: CSP plant characteristics

Parameter		Value
Rated power	P_{CSP}	$56\mathrm{MW}$
Power block efficiency	$\eta_{ ext{PB}}$	0.35
Solar field arrays	$n_{ m array}$	30
Heliostats per array	$n_{ m hel}$	2389
Lifetime	LT	30 years

It is assumed that all heliostat arrays exhibit identical behavior, described by a reference solar field. This solar field is associated to a flat plate receiver, and its characteristics are outlined in **Table 10**. Additionally, **Table 11** provides a summary of the heliostats properties.

Table 10: Receiver characteristics

Parameter		Value
Maximum power	$Q^{ m threshold}$	$10\mathrm{MW}$
Tower height	h_{tower}	$52\mathrm{m}$
Receiver length	$l_{ m rec}$	$4.5\mathrm{m}$
Receiver height	$h_{ m rec}$	4.5 m
Receiver zenith	$ heta_{ m rec}$	$-35\deg$
Receiver azimuth	$\gamma_{ m rec}$	$180\deg$
Absorbance	α	0.94
Thermal power loss	Q^{loss}	0.91 MW

Table 11: Heliostat characteristics

Parameter		Value
Heliostat height	$h_{ m hel}$	$2\mathrm{m}$
Heliostat width	$w_{ m hel}$	3.2 m
Reflective surface ratio	$ ho_{ m SR}$	0.97
Nominal reflectance	ρ	0.956
Stow angle	$\theta_{ m stow}$	$10\deg$
Stow tilt	$ heta_{ m tilt}$	90 deg

3.1. Solar field configurations

Starting from the reference modular solar field, that from now on will be addressed as base case, several solar field layouts are defined (refer to **Figure 8**). First, the undersized solar field layout is created by removing heliostats from the base case to prevent defocusing throughout the year. The worst-case scenario is considered, assuming pristine field conditions. For the base case pristine solar field, the most critical condition occurs on July 21st at 12 p.m., when 200 heliostats are defocused. Through a trial-and-error procedure, heliostats are removed from the edges of the base case layout until defocusing no longer occurs. In **Figure 8**, the layout of the undersized solar field is depicted and corresponds to the pink heliostats. On the other hand, the first oversized solar field layout is generated by adding to the base case the same approximate number of heliostats that were removed in the undersized solar field. The same procedure is followed to create the other oversized layouts, shown in **Figure 8**. The red, orange, yellow, green, blue and purple heliostats are added to get the oversized, oversized - 2, oversized - 3, oversized - 4, oversized - 5, and oversized - 6 configuration, respectively.

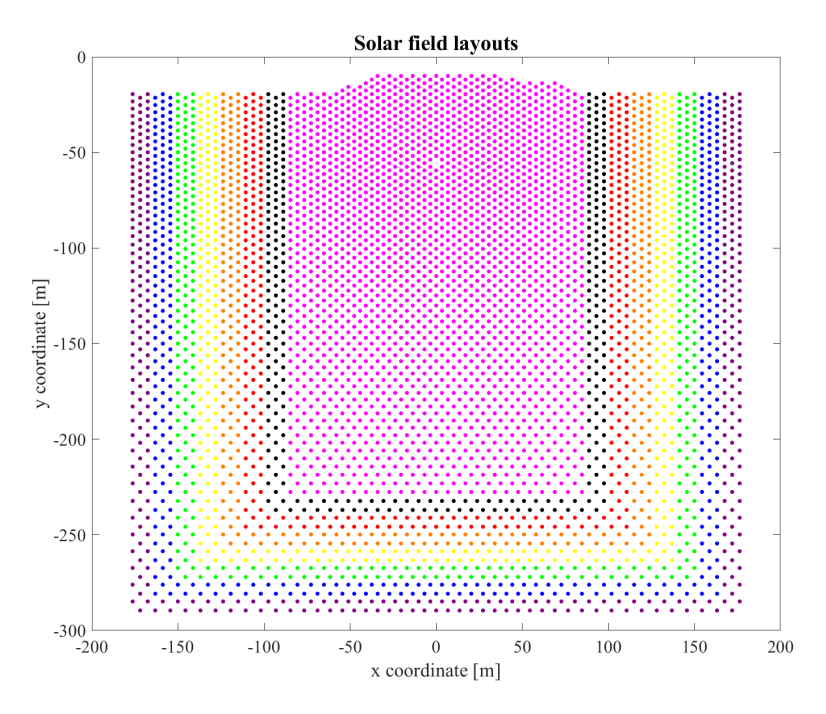


Figure 8: Solar field layouts

The solar field layouts are characterized by the following parameters.

Total reflective area of the solar field. The total reflective area, $A_{\rm sf}$, is the product of the heliostat area, $A_{\rm hel}$, the number of heliostats in the solar field, $n_{\rm hel}$, and the reflective surface ratio, $\rho_{\rm SR}$.

$$A_{\rm sf} = A_{\rm hel} \cdot n_{\rm hel} \cdot \rho_{\rm SR} \tag{64}$$

Solar Field Oversizing factor (SFO). The Solar Field Oversizing factor indicates the solar field oversizing with respect to the receiver. It is defined as the ratio between the power reflected on the receiver surface at design conditions, $Q_{\text{rec,design}}$, and the maximum power, $Q_{\text{threshold}}$.

$$SFO = \frac{Q_{\text{rec,design}}}{Q_{\text{threshold}}} \tag{65}$$

The power reflected on the receiver at design condition is computed as shown in **Equation 66**. η_{design} is design field efficiency. The design condition corresponds to midday of the spring equinox, with a DNI of $950 \,\text{W/m}^2$. Pristine field conditions are considered, and all heliostats are focused.

$$Q_{\text{design}} = DNI_{\text{design}} \cdot A_{\text{sf}} \cdot \eta_{\text{design}} \tag{66}$$

Solar Multiple (SM). The Solar Multiple is the ratio between the net thermal power of the solar field arrays at design conditions, $Q_{\text{HTF, design}}$, and the thermal power to run the power block at rated power, $Q_{\text{HTF, PB, max}}$.

$$SM = \frac{Q_{\text{HTF, design}}}{Q_{\text{HTF, PB, max}}} \tag{67}$$

The power absorbed by the HTF at design conditions is computed considering the threshold receiver power and the constant thermal energy loss. $Q_{\rm HTF,\ design}$ and the SM are the same for all solar field layouts.

$$Q_{\text{HTF, design}} = (Q_{\text{threshold}} - Q_{\text{loss}}) \cdot n_{\text{array}}$$
(68)

In Table 12 the characteristics of the solar field layouts are summarized.

 $\mathbf{A}_{\mathrm{sf}}\left[\mathbf{m^2}\right]$ SFO [-] $\Delta N_{
m hel}$ Solar field layout N.heliostats SM [-] Undersized 2088 -301 388,869 0.87 1.59 Base 2389 0 444,927 1.00 1.59 2702 +313Oversized 503,220 1.09 1.59 Oversized 2 3027 +638563,748 1.20 1.59 Oversized 3 3364 +975626,511 1.31 1.59 Oversized 4 691,509 3713 +13241.42 1.59 Oversized 5 4074 758,742 ± 1685 1.52 1.59 Oversized 6 4447 +2058828,209 1.62 1.59

Table 12: Solar field layouts characteristics

4. Results

The algorithm elaborated in **Section 2.2** is employed with an hourly time step for both the base case solar field and the configurations described in **Section 3.1**. SolarPILOT's *Image Size Priority* and a heuristic defocusing strategy are executed to determine the hourly power reflected on the receiver surface for each individual array. This process is repeated for both pristine and soiled field conditions, with the soiling rate serving as input to SolarPILOT, obtained as outlined in **Section 2.3.1**.

Subsequently, the analysis extends to encompass the entire CSP plant, rather than just a single array. Initially, the cleaning strategy undergoes optimization with HelioSoil as detailed in Section 2.3.2. The optimal cleaning schedule is determined by varying the number of trucks used in cleaning activities and the cleaning frequency, aiming to minimize the total cleaning cost. Figure 9(a) and Figure 9(b) illustrate the total cleaning cost trend, along with the corresponding degradation and cleaning costs, in relation to the number of trucks (ranging from 1 to 3) and the frequency of cleanings, for the base case solar field. The TCC shows a general downward trend with slight fluctuations. These curves terminate at the maximum number of yeraly cleanings achievable with the given number of trucks. The minimum TCC value is marked by a red star, indicating 24 cleanings per year with 2 trucks as the optimal combination. Moreover, the total cleaning cost is composed of the sum of the cleaning cost, which increases with the number of trucks and cleanings, and the degradation cost, which decreases with the number of cleanings and exhibits a fluctuating pattern.

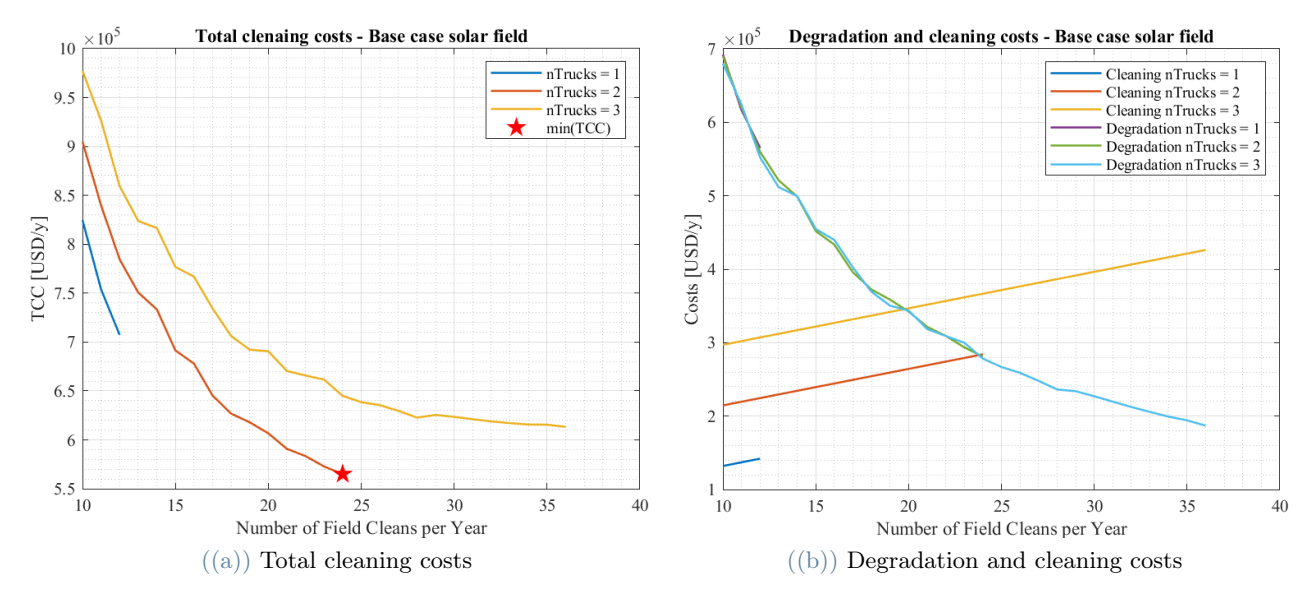


Figure 9: Total cleaning cost, cleaning cost and degradation cost, base case solar field

The same procedure is repeated for the other solar field configurations. **Table 13** summarizes the outcomes. The number of optimal trucks employed in the cleaning activities is stuck at two, while the frequency of yearly cleanings diminishes with the solar field size. The number of heliostats cleaned has a fluctuating downward trend, as well as the cleaning cost. The downward trend arises from the diminished cleaning capacity of a larger solar field, given the size of the cleaning fleet. On the other hand, the fluctuation stems from the adjusted cleaning speed, influenced by the length of the cleaning corridors and the time allocated for cleaning during the work shift. During a shift, more favourable layouts enable an extra corridor to be cleaned.

Table 13: Optimal cleaning strategy results

Field Layout	Optimal Trucks	$\begin{array}{c} \textbf{Optimal cleanings} \\ [\text{cleanings/year}] \end{array}$	${\bf Heliostats\ cleaned} \\ {\bf [heliostats/year]}$	$\begin{array}{c} \textbf{Cleaning cost} \\ [\text{USD/year}] \end{array}$
Undersized	2	30	1,753,920	306,434
Base	2	25	1,720,080	284,176
Oversized	2	21	1,702,260	293,117
Oversized 2	2	19	1,725,390	294,858
Oversized 3	2	17	1,614,720	294,124
Oversized 4	2	15	1,670,850	290,753
Oversized 5	2	13	1,588,860	280,943
Oversized 6	2	12	1,600,920	281,955

Furthermore, the drivers failure analysis is conducted according to **Section 2.4**. **Table 14** summarizes the outcomes. Ensuring the desired availability of heliostats necessitates a higher number of workers to address the growing number of malfunctioning drivers, consequently leading to increased repair costs.

Table 14: Drivers reliability and economic analysis results

Field Layout	$n_{ m hel}$	$n_{ m hel,tot}$	$n_{ m hel,down,tot}$	$n_{ m workers}$	$\mathbf{C_{repairs}}$ [USD/year]
Undersized	2,088	62,640	1,879	3.73	1,451,219
Base	2,389	71,670	2,150	4.27	1,533,501
Oversized 1	2,702	81,060	2,432	4.82	1,619,063
Oversized 2	3,027	90,810	2,724	5.40	1,707,905
Oversized 3	3,364	100,920	3,028	6.01	1,800,028

Oversized 4	3,713	111,390	3,342	6.63	1,895,431
Oversized 5	4,074	122,220	3,667	7.27	1,994,115
Oversized 6	4,447	133,410	4,002	7.94	2,096,078

Both cleaning strategy optimization and drivers failure analysis facilitate the identification of additional O&M costs to be included in the final economic assessment and contribute to penalizing the energy collected on the receiver. Moreover, the total energy absorbed by the HTF is computed in accordance with **Section 2.5**, and the electricity produced is determined based on the selected dispatching strategy, whether full-load or load-based turbine operation. The LCOE analysis encompasses exploration of various TES size couplings. In **Section 4.1** and **Section 4.2** the results for the two available dispatching strategies are detailed.

4.1. Full Load Operation Results

Figure 10(a) and Figure 10(b) show the trend of the LCOE as a function of the TES size for each solar field configuration, respectively considering pristine and soiled field conditions. These curves are characterized by a minimum LCOE: the corresponding TES size represents the optimal one because it leads to the most cost-effective TES-coupling, balancing costs and electricity production.

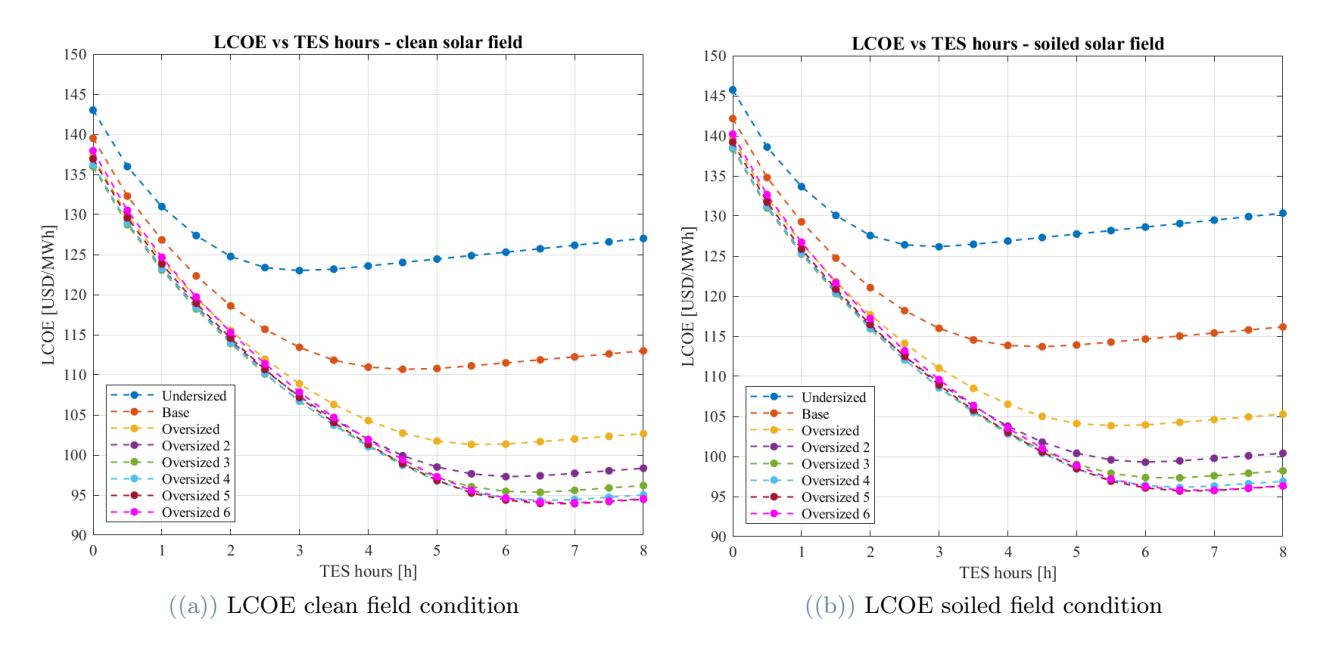


Figure 10: LCOE vs TES size, clean and soiled solar fields, full-load operation

The minimum LCOEs for each heliostat field configuration can be compared to determine the global minimum, thereby identifying the optimal solar field size, as illustrated in **Figure 11** where the optimal configuration is indicated by a star. The corresponding optimal TES hours, yearly electricity production, percentage energy loss, CAPEX and OPEX are summarized in **Table 15** and **Table 16**. In **Table 17** and **Table 18** CAPEX and OPEX costs breakdown are shown, for clean and soiled solar fields respectively. Differences are highlighted.

The minimum LCOE trend initially exhibits a sharp decline, which gradually levels off until reaching the minimum. Within this range, the LCOE experiences slight fluctuations among the configurations, indicating that an increase in the number of heliostats results in only marginal improvements in LCOE reduction. In general, given a solar field layout, the LCOE increases when considering soiled field conditions, primarily due to the electricity production penalization and the additional cleaning costs, which must be accurately accounted for in a comprehensive techno-economic assessment. However, under turbine full-load operation, the Oversized 5 configuration consistently achieves the minimum LCOE, regardless of whether clean or soiled conditions are considered. A marginal 1.8% increase in the optimal LCOE is noted when soiled conditions are taken into account. Correspondingly, the optimal TES hours, which typically scale with the solar field size, are 7.0 and 6.5 hours for clean and soiled fields, respectively. Considering soiling during the design phase, in fact, results in a reduction in the electricity production, and therefore a smaller TES size is required.

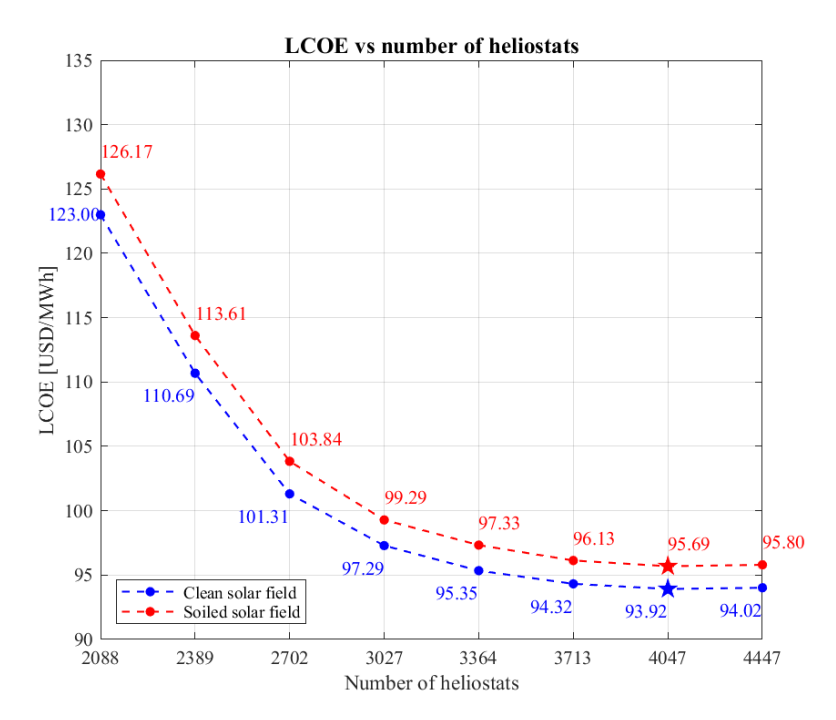


Figure 11: Optimal LCOEs, clean and soiled solar fields, full-load operation

Table 15: Minimum LCOEs, corresponding TES hours, and indicators. Pristine field condition

Clean Field Condition							
Field Layout	LCOE min [USD/MWh]	TES hours	EE [MWh]	$\mathbf{e_{loss,tot}}$	CAPEX [MUSD]	OPEX [MUSD/year]	
Undersized	123.00	3.0	171,049	0.23%	449.6	6.1	
Based	110.69	4.5	195,967	0.46%	462.7	6.3	
Oversized	101.31	5.5	219,867	3.15%	473.9	6.5	
Oversized 2	97.29	6.0	233,796	7.85%	483.1	6.6	
Oversized 3	95.35	6.5	243,397	12.61%	492.6	6.8	
Oversized 4	94.32	6.5	250,114	17.26%	500.2	6.9	
Oversized 5	93.92	7.0	256,148	21.14%	510.3	7.0	
Oversized 6	94.02	7.0	260,084	24.93%	518.4	7.2	

Table 16: Minimum LCOEs, corresponding TES hours, and indicators. Soiled field condition

	Soiled Field Condition								
Field Layout	$\begin{array}{c} \textbf{LCOE min} \\ [\text{USD/MWh}] \end{array}$	TES hours [h]	EE [MWh]	${ m e_{loss,tot}} \ { m [-]}$	CAPEX [MUSD]	$\begin{array}{c} \mathbf{OPEX} \\ [\mathrm{MUSD/year}] \end{array}$			
Undersized	126.17	3.0	169,110	0.12%	449.6	6.3			
Based	113.61	4.5	193,291	0.27%	462.7	6.5			
Oversized	103.84	5.5	217,201	2.56%	473.9	6.8			
Oversized 2	99.29	6.0	231,964	6.94%	483.1	6.9			
Oversized 3	97.33	6.5	241,339	11.52%	492.6	7.1			
Oversized 4	96.13	6.5	248,325	15.90%	500.2	7.2			
Oversized 5	95.69	6.5	253,434	20.01%	508.1	7.3			
Oversized 6	95.80	7.0	258,072	23.35%	518.4	7.4			

Table 17: CAPEX and OPEX breakdown, clean solar field

	Layout	Under.	Base	Over.	Over.2	Over.3	Over.4	Over.5	Over.6
	Tower	81.0	81.0	81.0	81.0	81.0	81.0	81.0	81.0
	Receiver	146.9	146.9	146.9	146.9	146.9	146.9	146.9	146.9
	Site imp.	6.2	7.1	8.1	9.0	10.0	11.1	12.1	13.3
SD	Solar field	25.7	29.4	33.2	37.2	41.3	45.6	50.1	54.7
MU	ВОР	16.2	16.2	16.2	16.2	16.2	16.2	16.2	16.2
\mathbf{CAPEX} [MUSD]	PC	58.2	58.2	58.2	58.2	58.2	58.2	58.2	58.2
4PE	TES	10.6	15.8	19.4	21.1	22.9	22.9	24.6	24.6
ŭ	Cont.	24.1	24.8	25.4	25.9	26.4	26.7	27.2	27.6
	Land	17.0	17.7	18.5	19.2	20.1	21.0	21.9	22.9
	Sales tax	15.6	16.1	16.5	16.8	17.1	17.4	17.8	18.0
	EPC	48.0	49.3	50.5	51.4	52.4	53.1	54.1	54.9
	Fixed	3.7	3.7	3.7	3.7	3.7	3.7	3.7	3.7
$egin{aligned} \mathbf{OPEX} \ [\mathrm{USD/y}] \end{aligned}$	Variable	0.9	1.0	1.2	1.2	1.3	1.3	1.4	1.4
OP [US]	Cleaning	0.0	0.0	0.0	0.0	0.0	0.0	0.0	0.0
	Repair	1.5	1.5	1.6	1.7	1.8	1.9	2.0	2.1

Table 18: CAPEX and OPEX breakdown, soiled solar field

	Layout	Under.	Base	Over.	Over.2	Over.3	Over.4	Over.5	Over.6
	Tower	81.0	81.0	81.0	81.0	81.0	81.0	81.0	81.0
	Receiver	146.9	146.9	146.9	146.9	146.9	146.9	146.9	146.9
	Site imp.	6.2	7.1	8.1	9.0	10.0	11.1	12.1	13.3
SD	Solar field	25.7	29.4	33.2	37.2	41.3	45.6	50.1	54.7
CAPEX [MUSD]	ВОР	16.2	16.2	16.2	16.2	16.2	16.2	16.2	16.2
X:	PC	58.2	58.2	58.2	58.2	58.2	58.2	58.2	58.2
^PE	TES	10.6	15.8	19.4	21.1	22.9	22.9	22.9	24.6
Ď	Cont.	24.1	24.8	25.4	25.9	26.4	26.7	27.1	27.6
	Land	17.0	17.7	18.5	19.2	20.1	21.0	21.9	22.9
	Sales tax	15.6	16.1	16.5	16.8	17.1	17.4	17.7	18.0
	EPC	48.0	49.3	50.5	51.4	52.4	53.1	53.9	54.9
	Fixed	3.7	3.7	3.7	3.7	3.7	3.7	3.7	3.7
$egin{aligned} \mathbf{OPEX} \ [\mathrm{USD/y}] \end{aligned}$	Variable	0.9	1.0	1.2	1.2	1.3	1.3	1.3	1.4
OP [US:	Cleaning	0.3	0.3	0.3	0.3	0.3	0.3	0.3	0.3
	Repair	1.5	1.5	1.6	1.7	1.8	1.9	2.0	2.1

4.2. Load-Based Operation Results

The minimum LCOEs trend is obtained as per **Section 4.1**. A comparison between the results in full-load and load-based operation in shown in **Figure 12(a)** and **Figure 12(b)**. The corresponding optimal TES hours, yearly electricity production, percentage energy loss, CAPEX and OPEX are summarized in **Table 19** and **Table 20**.

The minimum LCOE trend is the same experinced in full-load operation. Furthermore, in the load-based operation scenario, electricity production decreases while energy dissipation increases compared to full load operation. This decline in electricity production is attributed to the turbine not operating at full load, while the

increase in energy dissipation results from limiting electricity production during the day and shifting it towards the night. Consequently, the minimum LCOE is higher for each solar field configuration. The corresponding TES size increases to accommodate fluctuations in the load curve and the requirement to fulfill nighttime demand. Combining these factors, the minimum LCOE is consistently achieved for the Oversized 4 configuration, regardless of whether the layout is pristine or soiled. A slight 1.6% increase in the LCOE is observed when considering soiled field conditions. However, the corresponding optimal TES hours remain constant at 11.5.

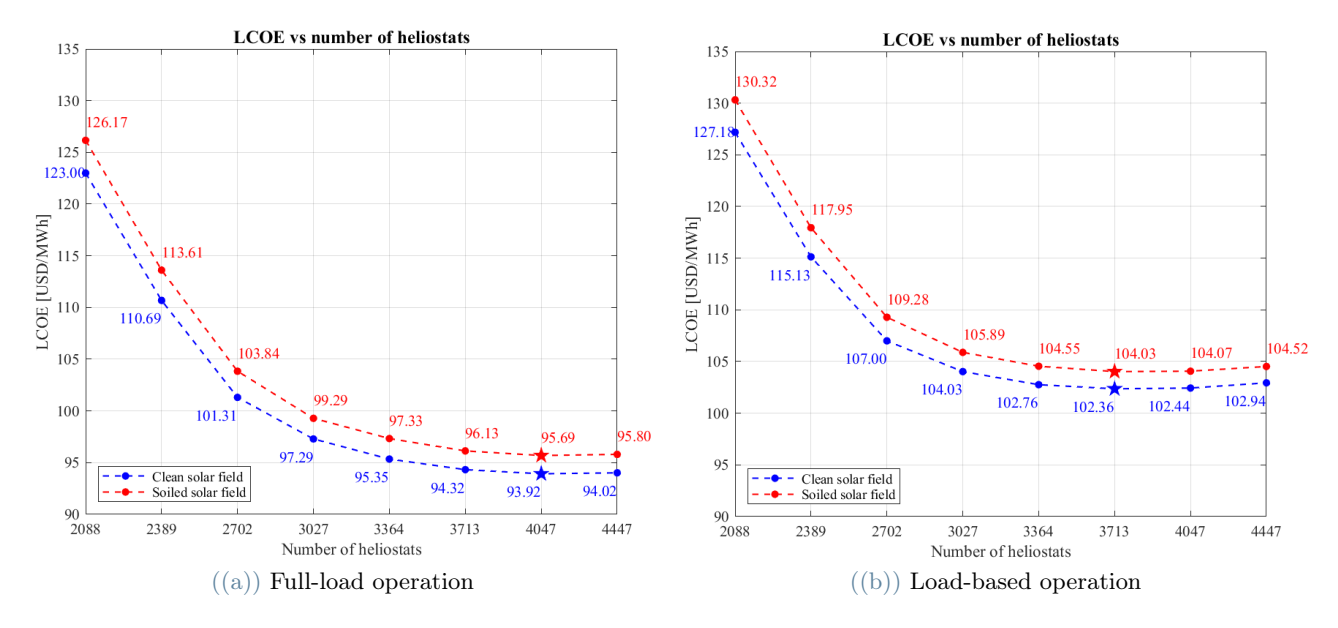


Figure 12: Minimum LCOEs a function of the number of heliostst

Table 19: Minimum LCOEs, corresponding TES hours, and indicators. Pristine field condition

Clean Field Condition								
Field Layout	$\begin{array}{c} \textbf{LCOE min} \\ [\text{USD/MWh}] \end{array}$	TES hours	EE [MWh]	e _{loss,tot}	CAPEX [MUSD]	OPEX [MUSD/year]		
Undersized	127.18	7.5	170,605	0.49%	469.4	6.1		
Based	115.13	9.0	194,055	1.43%	482.5	6.3		
Oversized	107.00	10.5	214,785	5.46%	495.9	6.5		
Oversized 2	104.03	11.0	225,287	11.49%	505.1	6.6		
Oversized 3	102.76	11.5	232,408	17.12%	514.7	6.7		
Oversized 4	102.36	11.5	236,962	22.50%	522.3	6.8		
Oversized 5	102.44	11.5	240,501	27.24%	530.1	7.0		
Oversized 6	102.94	12.0	243,836	31.17%	540.5	7.1		

Table 20: Minimum LCOEs, corresponding TES hours, and indicators. Soiled field condition

Soiled Field Condition							
Field Layout	$\begin{array}{c} \textbf{LCOE min} \\ [\text{USD/MWh}] \end{array}$	TES hours [h]	EE [MWh]	${ m e_{loss,tot}} \ { m [-]}$	CAPEX [MUSD]	$\begin{array}{c} \mathbf{OPEX} \\ [\mathrm{MUSD/year}] \end{array}$	
Undersized	130.32	7.5	168,781	0.32%	469.4	6.3	
Based	117.95	8.5	191,071	1.42%	480.3	6.5	
Oversized	109.28	10.0	212,187	4.87%	493.7	6.7	
Oversized 2	105.89	11.0	224,047	10.35%	505.1	6.9	
Oversized 3	104.55	11.5	231,197	15.72%	514.7	7.0	

Oversized 4	104.03	11.5	235,909	20.10%	522.3	7.1
Oversized 5	104.07	11.5	239,373	25.54%	530.1	7.2
Oversized 6	104.52	11.5	242,049	29.55%	538.3	7.4

4.3. Comparison

Depending on the dispatching scenario, the optimal solar field size varies: Oversized 5 is the best configuration for full-load turbine operation, while Oversized 4 is preferred for load-based operation. In **Table 21**, the minimum LCOEs and the corresponding TES sizes are summarised.

Table 21: LCOE and TES sizes summary

	F	ıll load operati	on	Load based operation		
	Solar field layout				$\begin{array}{c} \mathbf{min} \ \mathbf{LCOE} \\ [\mathrm{USD/MWh}] \end{array}$	TES hours [h]
Clean field	Oversized 5	93.92	7.0	Oversized 4	102.36	11.5
Soiled field	Oversized 5	95.69	6.5	Oversized 4	104.03	11.5

Figure 13 compares electricity production under clean and soiled conditions for these two optimal configurations. Full-load dispatching results in higher electricity production in both clean and soiled conditions, thanks to the larger solar field oversizing and turbine operation at nominal conditions. Conversely, load-based dispatching requires a smaller solar field to meet reduced electricity demand.

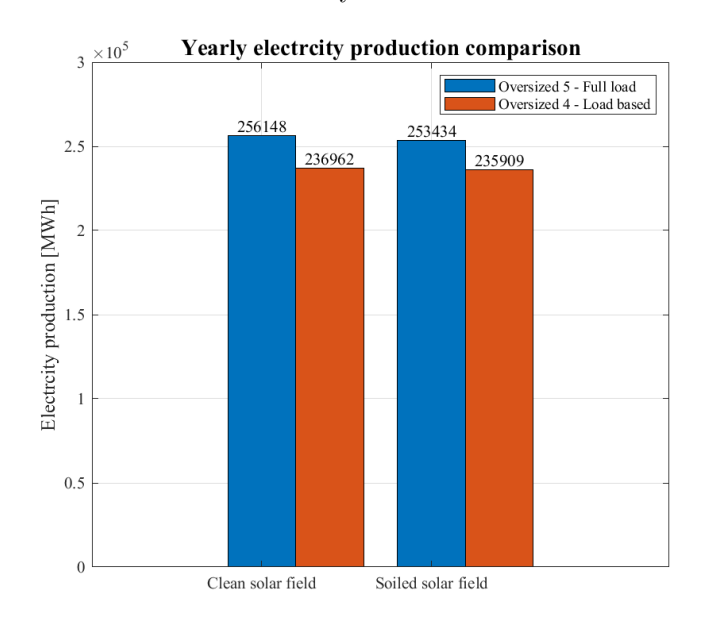


Figure 13: Electricity production comparison

Figure 14(a) and Figure 14(b) compare CAPEX and OPEX for the optimal layouts, considering soiled field conditions (worst case scenarios), for both dispatching options. Apart from variable production-based costs, the primary distinction lies in the heliostat field cost and the storage cost, with the TES size being nearly twice as large in the load-based scenario. A proper selection of the TES size should be based on the expected operational profile of the power plant throughout its lifetime. In the design phase, considerations must include worst-case scenarios, such as a soiled solar field, to factor in cleaning costs and reduced electricity production.

The receiver cost stands out as notably higher compared to other components. This disparity stems from the reference values utilized in **Equation 50** and summerized in **Table 7**, which are calibrated for larger-surface receivers. While aligning with SAM's standards, it is chosen to maintain this approach. Nevertheless, future research could delve into a more detailed analysis of receiver costs.

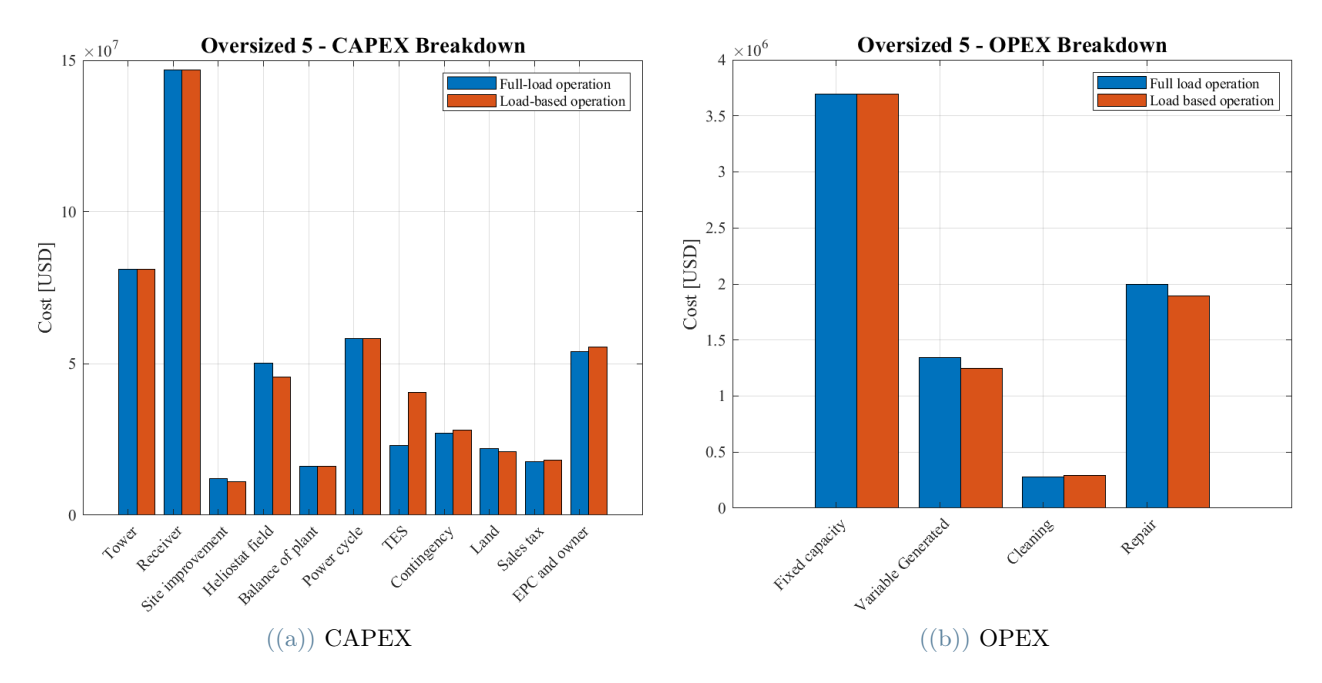


Figure 14: CAPEX and OPEX comparison

5. Sensitivity Analysis

In this section a sensitivity analysis on the heliostats price is performed. The starting price, $66\,\mathrm{USD/m^2}$, is low with respect to average values, $127\,\mathrm{USD/m^2}$ as stated by SAM [50], shifting the optimal solution towards larger solar fields. The goal is exploring the effect of heliostats price increase on the solar field layout selection.

Figure 15 shows the trend of the minimum LCOEs as a function of the number of heliostats in the solar field, for clean and soiled conditions, when the heliostats price varies from $66\,\mathrm{USD/m^2}$ to $125\,\mathrm{USD/m^2}$. The full-load dispatching strategy is selected. The optimal solutions are indicated by the stars: as the price of heliostats increases, the optimal configuration shifts towards smaller fields. Specifically, when the heliostats price reaches $125\,\mathrm{USD/m^2}$, the optimal configuration shifts from a five-fold oversized field to a four-fold oversized solar field. Across all optimal configurations, the coupled storage size remains fixed at 6.5 hours.

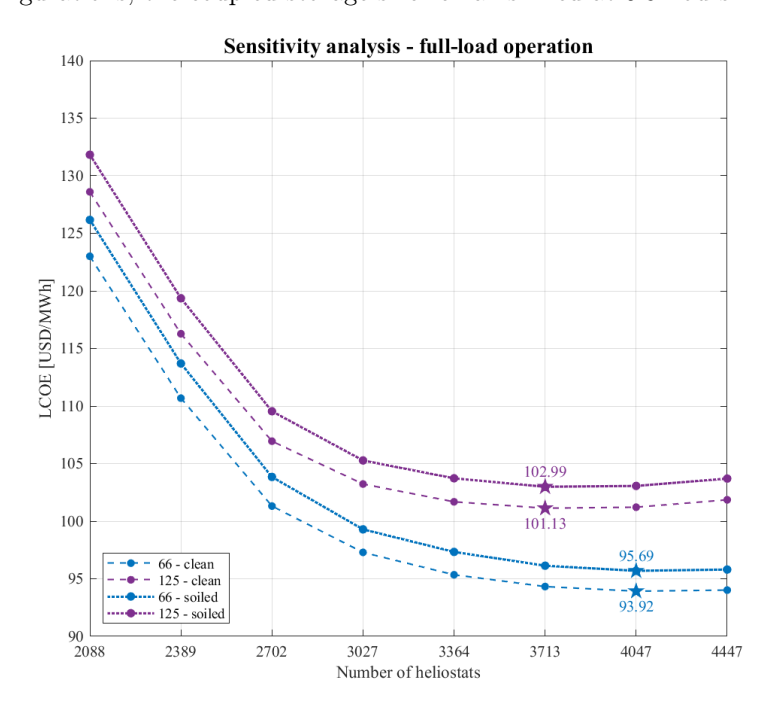


Figure 15: Sensitivity analysis, clean and soiled solar fields, full-load operation

Figure 16 shows the trend of the minimum LCOEs as a function of the number of heliostats in the solar fields,

for clean and soiled conditions respectively, when the heliostats price varies from $66\,\mathrm{USD/m^2}$ to $125\,\mathrm{USD/m^2}$. The load-based dispatching strategy is selected. Consistently, when the heliostat price reaches $125\,\mathrm{USD/m^2}$, it triggers a transition from a four-fold oversized field to a three-fold oversized solar field in the optimal configuration. The coupled storage size remains constant at 11.5 hours.

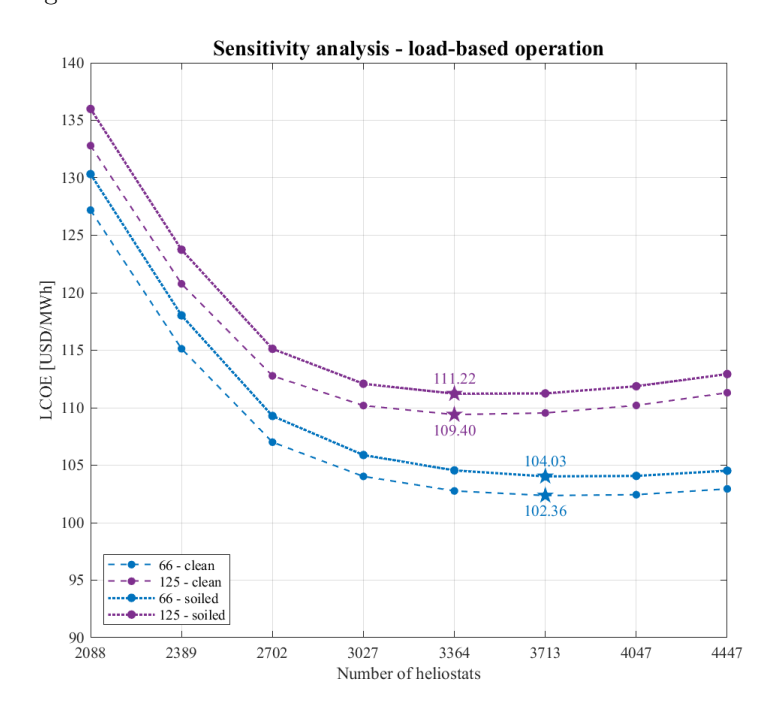


Figure 16: Sensitivity analysis, clean and soiled solar fields, load-based operation

The sensitivity analysis provides insights into the reasons behind the shift towards highly oversized solar fields when considering a base heliostat price of $66\,\mathrm{USD/m^2}$. When a price more in line with average values is taken into account, the optimal configurations for the full load scenario would involve a four-times oversized solar field, coupled with a 6.5-hour TES. Similarly, for the load-based scenario, a three-times oversized solar field, coupled with an 11.5-hour TES, would be optimal. Results are summarized in **Table 22**.

	F	ull load operati	on	Load based operation		
	Solar field layout	$\begin{array}{c} \mathbf{min} \ \mathbf{LCOE} \\ [\mathrm{USD/MWh}] \end{array}$	TES hours [h]	Solar field layout	$\begin{array}{c} \mathbf{min} \ \mathbf{LCOE} \\ [\mathrm{USD/MWh}] \end{array}$	TES hours [h]
Clean field	Oversized 4	101.13	6.5	Oversized 3	109.40	11.5
Soiled field	Oversized 4	102 99	6.5	Oversized 3	111 22	11.5

Table 22: LCOE and TES sizes summary, sensitivity analysis

The minimum LCOE experiences a 7.5% increase in full-load operation and a 7% increase in load-based operation, regardless of whether the conditions are clean or soiled. The optimal TES hours remain unchanged.

6. Conclusions

In this study, a methodology for preliminary sizing the heliostat field of Solar Tower power plants is outlined, aiming to achieve the best techno-economic compromise. This approach is comprehensive, integrating several factors into the optimization procedure.

Initially, heliostat tracking is considered, with SolarPILOT's *Image Size Priority* chosen as the designated aiming strategy to evenly distribute thermal flux across the receiver surface. To adhere to the limit on maximum power collected on the receiver, a custom defocusing and re-focusing strategy is implemented. Heliostats are defocused and re-focused in groups of 8 and 4, respectively, until the constraint is met.

Soiling losses are then addressed in two ways: firstly, a validated physical model quantifies the heliostat soiling rate, which is ultimately meant for penalizing the field optical efficiency and, consequently, the power collected on the receiver. Secondly, the heliostat cleaning strategy is optimized in terms of the number of deployed trucks and cleaning frequency, with resulting cleaning costs factored into O&M cost calculations.

Additionally, a drivers failure analysis is conducted to penalize the power production based on the heliostat availability and calculate additional O&M costs due to heliostat repairs.

The electric energy production by the CSP plant is computed under two dispatching options: turbine full-load operation and residual load-curve based operation. The former involves running the turbine at nominal power whenever possible, either using the power absorbed by the HTF or draining the TES. The latter entails adjusting the turbine production to follow a pre-specified residual load curve.

This methodology is applied to a CSP facility in Mount Isa, Queensland, Australia, consisting of 30 heliostat arrays. A modular solar field (base case) serves as reference to define further layouts, including an undersized layout with no defocusing throughout the year and six oversized layouts. For each solar field layout - TES hours combination, the LCOE is computed and the minimum values compared to find the globally optimal solution. During the design phase, worst-case scenario considerations dictate the use of soiling conditions as a reference.

The results indicate that, for turbine full-load operation, the optimal configuration is a five-times oversized solar field coupled with a 6.5-hour TES, resulting in an LCOE of 95.69 USD/MWh. Conversely, for turbine load-based operation, the optimal configuration is an four-times oversized solar field with an 11.5-hour TES, resulting in a LCOE of 93.92 USD/MWh. Design choices should be influenced by the expected turbine operation throughout its lifetime.

Lastly, a sensitivity analysis on heliostats price is conducted. When the price increases from the base value of $66\,\mathrm{USD/m^2}$ to average commercial values of $125\,\mathrm{USD/m^2}$, the optimal solar field size diminishes. For full-load operation, the optimal LCOE becomes $102.99\,\mathrm{USD/MWh}$, corresponding to a four-times oversized solar field. For load-based operation, the optimal LCOE becomes $111.22\,\mathrm{USD/MWh}$, corresponding to a three-times oversized field. The optimal TES size remains unchanged.

In conclusion, this research demonstrates how to define and apply a preliminary solar field design methodology to a real case study. Further developments could include integrating more sophisticated aiming strategies, such as HALOS, as the NREL is resolving inconsistencies in the software to make it useful for future research. Additionally, refining solar field layouts by considering not only the size but also the shape and placement of heliostats could lead to further improvements.

References

- [1] IRENA. World energy transitions outlook 2023: 1.5°c pathway. Technical report, International Renewable Energy Agency, 2023.
- [2] IRENA. Renewable power generation costs in 2022. Technical report, International Renewable Energy Agency, 2023.
- [3] Travis Sarver, Ali Al-Qaraghuli, and Lawrence L. Kazmerski. A comprehensive review of the impact of dust on the use of solar energy: History, investigations, results, literature, and mitigation approaches. Renewable and Sustainable Energy Reviews, 22:698–733, 2013.
- [4] Alberto Sánchez-González, María Reyes Rodríguez-Sánchez, and Domingo Santana. Allowable solar flux densities for molten-salt receivers: Input to the aiming strategy. *Results in Engineering*, 5:100074, 2020.
- [5] Gabriela de Andrade Oliveira Ígor Marques Alves Magdalena Marta Walczak Cristiana Brasil Maia, Lucas Rodrigues Neumann and Pedro Paiva Brito. A comprehensive review of solar tower csp systems using tes and molten salts. *International Journal of Ambient Energy*, 44(1):1733–1747, 2023.
- [6] Zaharaddeen Ali Hussaini, Peter King, and Chris Sansom. Numerical Simulation and Design of Multi-Tower Concentrated Solar Power Fields. *Sustainability*, 12(6):1–22, March 2020.
- [7] Arslan A. Rizvi, Syed N. Danish, Abdelrahman El-Leathy, Hany Al-Ansary, and Dong Yang. A review and classification of layouts and optimization techniques used in design of heliostat fields in solar central receiver systems. Solar Energy, 218:296–311, 2021.
- [8] Francisco J. Collado and Jesus Guallar. Quick design of regular heliostat fields for commercial solar tower power plants. *Energy*, 178:115–125, 2019.
- [9] Chao Li, Rongrong Zhai, and Yongping Yang. Optimization of a heliostat field layout on annual basis using a hybrid algorithm combining particle swarm optimization algorithm and genetic algorithm. *Energies*, 10(11), 2017.

- [10] Jianxing Wang, Liqiang Duan, Yongping Yang, and Laishun Yang. Rapid design of a heliostat field by analytic geometry methods and evaluation of maximum optical efficiency map. Solar Energy, 180:456–467, 2019.
- [11] Salhi S. Redondo J.L. et al. Cruz, N.C. Design of a parallel genetic algorithm for continuous and pattern-free heliostat field optimization. *The Journal of Supercomputing*, 2019.
- [12] Libao Deng, Yiran Wu, Su Guo, Lili Zhang, and Haili Sun. Rose pattern for heliostat field optimization with a dynamic speciation-based mutation differential evolution. *International Journal of Energy Research*, 44(3):1951–1970, 2020.
- [13] Mohammad Saghafifar, Mohamed Gadalla, and Kasra Mohammadi. Thermo-economic analysis and optimization of heliostat fields using aineh code: Analysis of implementation of non-equal heliostats (aineh). Renewable Energy, 135:920–935, 2019.
- [14] Peter Schöttl, Shahab Rohani, Erminia Leonardi, Lorenzo Pisani, Iñigo Les, Amaia Mutuberria, and Peter Nitz. Solar field heliostat selection based on polygon optimization and boundaries. AIP Conference Proceedings, 2126(1):030053, 07 2019.
- [15] Seonghyeok Yang, Kyungeun Lee, and Ikjin Lee. Pattern-free heliostat field layout optimization using physics-based gradient. *Solar Energy*, 206:722–731, 2020.
- [16] Elisa Ghirardi, Giovanni Brumana, Giuseppe Franchini, and Antonio Perdichizzi. Heliostat layout optimization for load-following solar tower plants. *Renewable Energy*, 168:393–405, 2021.
- [17] Lorin L. Vant-Hull. The role of "allowable flux density" in the design and operation of molten-salt solar central receivers. *Journal of Solar Energy Engineering, Transactions of the ASME*, 124:165–169, 5 2002.
- [18] Alberto Sánchez-González, María Reyes Rodríguez-Sánchez, and Domingo Santana. Aiming strategy model based on allowable flux densities for molten salt central receivers. *Solar Energy*, 157:1130–1144, 11 2017.
- [19] Alberto Sánchez-González, María Reyes Rodríguez-Sánchez, and Domingo Santana. Aiming factor to flatten the flux distribution on cylindrical receivers. *Energy*, 153:113–125, 6 2018.
- [20] Jesús García, Yen Chean Soo Too Ricardo Vasquez Padilla, and Rodrigo Barraza Vicencio Andrew Beath Marco Sanjuan. Heat flux distribution over a solar central receiver using an aiming strategy based on a conventional closed control loop. 2017.
- [21] N.C. Cruz, J.L. Redondo, J.D. Álvarez, M. Berenguel, and P.M. Ortigosa. On achieving a desired flux distribution on the receiver of a solar power tower plant. pages 61–64.
- [22] Adrien Salomé, Fabien Chhel, Gilles Flamant, Alain Ferrière, and Frederik Thiery. Control of the flux distribution on a solar tower receiver using an optimized aiming point strategy: Application to themis solar tower. Solar Energy, 94:352–366, 8 2013.
- [23] Saeb M. Besarati, D. Yogi Goswami, and Elias K. Stefanakos. Optimal heliostat aiming strategy for uniform distribution of heat flux on the receiver of a solar power tower plant. Energy Conversion and Management, 84:234–243, 2014.
- [24] Boris Belhomme, Robert Pitz-Paal, and Peter Schwarzbözl. Optimization of heliostat aim point selection for central receiver systems based on the ant colony optimization metaheuristic. *Journal of Solar Energy Engineering, Transactions of the ASME*, 136, 2014.
- [25] Laurin Oberkirsch, Daniel Maldonado Quinto, Peter Schwarzbözl, and Bernhard Hoffschmidt. Gpu-based aim point optimization for solar tower power plants. Solar Energy, 220:1089–1098, 5 2021.
- [26] Marco Astolfi, Marco Binotti, Simone Mazzola, Luca Zanellato, and Giampaolo Manzolini. Heliostat aiming point optimization for external tower receiver. *Solar Energy*, 157:1114–1129, 11 2017.
- [27] Thomas Ashley, Emilio Carrizosa, and Enrique Fernández-Cara. Optimisation of aiming strategies in solar power tower plants. *Energy*, 137:285–291, 2017.
- [28] et al. Zhu, Guangdong. Roadmap to advance heliostat technologies for concentrating solar-thermal power. Technical report, Golden, CO: National Renewable Energy Laboratory, 2022.

- [29] D.J. Griffith, L. Vhengani, and M. Maliage. Measurements of mirror soiling at a candidate csp site. *Energy Procedia*, 49:1371–1378, 2014. Proceedings of the SolarPACES 2013 International Conference.
- [30] A. Alami Merrouni, F. Wolfertstetter, A. Mezrhab, S. Wilbert, and R. Pitz-Paal. Investigation of soiling effect on different solar mirror materials under moroccan climate. *Energy Procedia*, 69:1948–1957, 2015. International Conference on Concentrating Solar Power and Chemical Energy Systems, SolarPACES 2014.
- [31] Ahmed Alami Merrouni, Ricardo Conceição, Ammar Mouaky, Hugo Gonçalves Silva, and Abdellatif Ghennioui. Csp performance and yield analysis including soiling measurements for morocco and portugal. Renewable Energy, 162:1777–1792, 2020.
- [32] S. Bouaddi, A. Ihlal, and A. Fernández-García. Soiled csp solar reflectors modeling using dynamic linear models. *Solar Energy*, 122:847–863, 2015.
- [33] S. Bouaddi, A. Ihlal, and A. Fernández-García. Comparative analysis of soiling of csp mirror materials in arid zones. *Renewable Energy*, 101:437–449, 2017.
- [34] Ricardo Conceição, Hugo G. Silva, and Manuel Collares-Pereira. Csp mirror soiling characterization and modeling. Solar Energy Materials and Solar Cells, 185:233–239, 2018.
- [35] Aristides M. Bonanos, Manuel J. Blanco, and Kypros Milidonis. Characterization of mirror soiling in CSP applications. AIP Conference Proceedings, 2303(1):030007, 12 2020.
- [36] G. Picotti, P. Borghesani, G. Manzolini, M. E. Cholette, and R. Wang. Development and experimental validation of a physical model for the soiling of mirrors for csp industry applications. *Solar Energy*, 173:1287–1305, 10 2018.
- [37] G. Picotti, P. Borghesani, M. E. Cholette, and G. Manzolini. Soiling of solar collectors modelling approaches for airborne dust and its interactions with surfaces, 1 2018.
- [38] Giovanni Picotti, Marco Binotti, Michael E. Cholette, Pietro Borghesani, Giampaolo Manzolini, and Ted Steinberg. Modelling the soiling of heliostats: Assessment of the optical efficiency and impact of cleaning operations. volume 2126. American Institute of Physics Inc., 7 2019.
- [39] K D Bergeron and J M Freese. Cleaning strategies for parabolic-trough solar-collector fields; guidelines for decisions.
- [40] Fabian Wolfertstetter, Stefan Wilbert, Jürgen Dersch, Simon Dieckmann, Robert Pitz-Paal, and Abdellatif Ghennioui. Integration of Soiling-Rate Measurements and Cleaning Strategies in Yield Analysis of Parabolic Trough Plants. *Journal of Solar Energy Engineering*, 140(4):041008, 04 2018.
- [41] H. Truong Ba, M.E. Cholette, R. Wang, P. Borghesani, L. Ma, and T.A. Steinberg. Optimal condition-based cleaning of solar power collectors. *Solar Energy*, 157:762–777, 2017.
- [42] Thomas Ashley, Emilio Carrizosa, and Enrique Fernández-Cara. Heliostat field cleaning scheduling for solar power tower plants: A heuristic approach. *Applied Energy*, 235:653–660, 2019.
- [43] Giovanni Picotti, Luca Moretti, Michael Cholette, Marco Binotti, Riccardo Simonetti, Emanuele Martelli, Theodore Steinberg, and Giampaolo Manzolini. Optimization of cleaning strategies for heliostat fields in solar tower plants. Solar Energy, 204:501–514, 07 2020.
- [44] Cody B. Anderson, Giovanni Picotti, Michael E. Cholette, Bruce Leslie, Theodore A. Steinberg, and Giampaolo Manzolini. Heliostat-field soiling predictions and cleaning resource optimization for solar tower plants. *Applied Energy*, 352:121963, 2023.
- [45] J. F. Nagel, Jr. Reliability study of solar one, the central receiver pilot plant.
- [46] Samir Benammar and Kong Fah Tee. Failure probability analysis of heliostat systems. *International Journal of Critical Infrastructures*, 16(4):342–366, 2020.
- [47] Alexander Zolan, William Hamilton, Kashif Liaqat, Michael Wagner, USDOE Office of Energy Efficiency, and Renewable Energy. Halos (heliostat aimpoint and layout optimization software), 6 2021.
- [48] Solarpilot.

- [49] Scott A Jones, Ronald Lumia, Roger Davenport, Robert C Thomas, David Gorman, Gregory J Kolb, and Matthew W Donnelly. Heliostat cost reduction study.
- [50] Janine Freeman Ty Neises Nate Blair, Aron P. Dobos and Michael Wagner. System advisor model, sam 2014.1.14: General description. Technical report, National Renewable Energy Laboratory, 2014.

Abstract in lingua italiana

Affinché gli impianti solari termici a torre vengano adottati su scala globale, alcune problematiche fondamentali dovranno essere affrontate, tra cui lo sporcamento degli eliostati. Questo fenomeno comporta perdite di efficienza ottica e costi di gestione e manutenzione aggiuntivi dovuti alla necessaria pulizia degli specchi. Altra sfida importante è la massimizzazione della potenza termica prodotta dal ricevitore, che dipende dalla strategia di mira selezionata, che a sua volta infleunza l'efficienza termica e la vita utile del ricevitore stesso.

In questo contesto, la presente ricerca propone una metodologia per ottimizzare il design preliminare del campo solare degli impianti solari a torre. Tale approccio integra un modello fisico per simulare le perdite dovute allo sporcamento degli eliostati e ottimizza la strategia di pulizia attraverso un metodo euristico tempo-basato e con frequenza fissata. Inoltre, viene introdotta un'analisi relativa ai possibili guasti degli eliostati.

Questa metodologia viene applicata all'impianto solare termico di Mount Isa, in Queensland, Australia. Sono prese in considerazione diverse dimensioni del campo solare al fine di identificare la configurazione con il minor Levelized Cost of Electrcity. I risultati indicano che un sovradimensionamento del campo solare di cinque volte, accoppiato a uno storage termico di 6.5 ore, è la soluzione ottimale quando la turbina viene operata a potenza nominale. Un sovradimensionamento di quattro volte, invece, accoppiato a uno storage termico di 11.5 ore, è la soluzione migliore quando la turbina è destinata a seguire una curva di carico predefinita. Un'analisi di sensitività sul prezzo degli eliostati mostra che le dimensioni ottimali del campo si riducono di una taglia quando i prezzi raddoppiano, indipendentemente dalla strategia operativa della turbina.

In conclusione, la ricerca proposta contribuisce allo sviluppo di una metodologia comprensiva per il dimensionamento del campo solare degli impianti a torre solare, integrando strategie di mira e considerazioni sullo sporcamento degli eliostati, e sottolineando l'influenza delle strategie di dispacciamento e del prezzo degli eliostati sull'economia e perfromance dell'impianto.

Parole chiave: CSP, torre solare, campo solare, sporcamento, pulizia degli eliostati, strategie di mira

Acknowledgements

Eccomi qui, a chiudere con questa tesi un percorso lungo cinque anni, a volte po' sofferto ma che mi ha regalato anche tante soddisfazioni.

Vorrei cominciare ringraziando il Prof. Giampaolo Manzolini per il supporto prezioso che mi ha offerto nello sviluppo di questa ricerca. La sua costante disponibilità e il costruttivo confronto instaurato nel corso di questi mesi sono stati fondamentali per il mio lavoro. Ho imparato tanto. Un ringraziamento va anche a tutto il team di ricerca che mi ha accolta al Queensland Univeristy of Technology e con cui ho avouto il piacere di lavorare, in particolar modo a prof. Michael Cholette, Dott. Giovanni Picotti e Mr. Cody Anderson, che mi ha seguita dai primissimi inizi con grande pazienza e attenzione.

Un grande grazie va alle persone con cui ho condiviso questo percorso, Luca B., Luca C., Livio, Ivan, Federica, Federico, Claudio, Simone e tanti altri. Siete stati dei fedeli compagni di avventure, risate e partite di carte clandestine in BL.27. Mi avete regalato tanti sorrisi.

Grazie alle mie miglioi amiche, Benedetta, Marianna, Giorgia e Federica. Mi avete accompagnata in questo percorso fin dagli inizi e mi avete sempre sostenuta, anche quando stavo dall'altra parte del mondo.

Grazie ad Alberto, con cui ho condiviso le gioie e le difficoltà di questo percorso. Abbiamo preso strade diverse proprio sul finale, ma se sono arrivata fin qui è anche grazie a te.

Infine grazie alla mia famiglia, in particolar modo ai miei genitori, Adriano e Roberta, e mio fratello Matteo. Grazie per avermi messo le ali e avermi permesso di realizzare i miei sogni, mi avete dato tutti gli strumenti di cui avevo bisogno e avete sempre creduto in me. Un grazie non basta, ne servirebbero mille. Vi voglio bene.

Dedico questa tesi a miei nonni, Mario e Livia, che durante la pandemia se ne sono andati e che sarebbero stati orgogliosi di vedermi raggiungere questo traguardo. Siete sempre con me.